Hydrothermal activity on the CV parent body: new perspectives from the giant Transantarctic Mountains minimeteorite TAM5.29

Nava J.[1] (*corresponding author*), Suttle M.D.[2,3], Spiess R.[1], Folco L[2], Najorka J.[3], Carli C.[4] and Massironi M[1] jacopo.nava@phd.unipd.it , martindavid.suttle@dst.unipi.it, richard.spiess@unipd.it, luigi.folco@unipi.it, j.najorka@nhm.ac.uk, cristian.carli@inaf.it, matteo.massironi@unipd.it.

[1.]University of Padova, Department of Geosciences, Via G.Gradenigo 6, 35131 Padova, Italy.
[2.]Dipartimento di Scienze della Terra, Università di Pisa, 56126 Pisa, Italy.
[3.]Core research laboratories, Department of Earth Science, The Natural History Museum, Cromwell Rd, London SW7 5BD, UK.
[4.]IAPS-INAF, Istituto Nazionale di Astrofisica e Planetologia Spaziali, Roma, Italy

Abstract

TAM5.29 is an extraterrestrial dust grain, collected on the Transantarctic Mountains (TAM). Its mineralogy is dominated by an Fe-rich matrix composed of platy fayalitic olivines and clasts of andradite surrounded by diopside-jarosite mantles, chondrules are absent. TAM5.29 records a complex geological history with evidence of extensive thermal metamorphism in presence of fluids at T<300°C. Alteration was terminated by an impact, resulting in shock melt veins and compaction-orientated foliation of olivine. A second episode of alteration at lower temperatures (<100°C) occurred post-impact and is either parent body or terrestrial in origin and resulted in the formation of iddingsite. The lack of chondrules is explained by random sub-sampling of the parent body, with TAM5.29 representing a matrix-only fragment. On the basis of bulk chemical composition, mineralogy and geological history TAM5.29 demonstrates affinities to the CV_{ox} group with a mineralogical assemblage in between the Allende-like and Bali-like subgroups (CV_{oxA} and TAM5.29 are rich in andradite, magnetite and FeNiS but CV_{oxA} lacks hydrated minerals, common in TAM5.29. Conversely CV_{oxB} are rich in hydrated phyllosilicates but contains almost pure fayalite, not found in TAM5.29). In addition, TAM5.29 has a slightly different metasomatic history, in-between the oxidised and reduced CV metamorphic grades whilst also recording higher oxidizing conditions as compared to the known CV chondrites. This study represents the third CV-like cosmic dust particle, containing a unique composition, mineralogy and fabric, demonstrating variation in the thermal metamorphic history of the CV parent body(-ies).

1. Introduction

The CV (Vigarano-like) carbonaceous chondrites (CCs) are a group of primitive meteorites sharing approximately equal ratios of chondrules and matrix, as well as the highest abundances of refractory phases (CAIs [Ca-Al-rich inclusions] and AOAs [ameboid olivine aggregate]) among any chondrite class (~10 vol%, McSween, 1977; Brearley and Jones, 1998; Weisberg et al., 2006). Chondrules in CVs are typically large (averaging 1 mm in diameter) type I, porphyritic olivine subtypes (~90%, Jones, 2012) and often surrounded by thick (~400µm) accretionary rims (King and King, 1991; Tomeoka and Ohnishi, 2010). Meanwhile, their matrices are rich in fayalitic olivine, Ca,Fe-pyroxenes and andradite (Krot et al., 1995-1998; Brearley and Jones, 1998; Weisberg et al., 2006).

The CV chondrite group most likely represent members of a single parent body, derived from an asteroid-sized planetesimal. Thermal remnant magnetism studies reveal a single coherent magnetic field among constituent chondrules (Carporzen et al., 2011). This requires the presence of a partially differentiated structure with a molten core and silicate mantle overlain by a cold chondritic "*lid*" as described by the model of Weiss and Elkins-Tanton, (2013). Furthermore, isotopic signatures of CV

chondrites ($\varepsilon^{54}Cr$ vs. $\varepsilon^{50}Ti$ and $\varepsilon^{54}Cr$ vs. $\Delta^{17}O$) fall within the carbonaceous supergroup, requiring an outer solar system origin or late accretion history (Warren, 2011). In addition to a partially differentiated interior, the CV chondritic "*lid*" attests to a protracted episode of parent body evolution with evidence for aqueous alteration (variously characterised by oxidation, hydration and replacement [e.g. phyllosilicate-rich chondrule rims, Tomeoka and Tanimura, 2000 or oxidized metal and mobilized Na and K, Krot et al., 2004]) as well as recording the highest grade shock deformation among the carbonaceous chondrites (commonly S2-S3 shock stages, Scott et al., 1992) and thermal metamorphism (~300°C, Krot et al., 1995; 1998).

The CV class is divided into two subgroups: a reduced (CV_{red}) and an oxidized group (CV_{ox}) – dependent on their ratio of metal/magnetite and on the Ni content of sulfide phases (Mcsween, 1977). The oxidised CVs are further classified into Bali-like (CV_{oxB}) and Allende-like (CV_{oxA}) subtypes, with the Bali-like population containing high abundances of hydrated minerals (up to 4.2 vol%, Howard et al., 2010) (including Fe-phyllosilicate) and nearly pure fayalite (Fa_{90}) (e.g. Kaba: Fo_{100}=20.9 vol% and Fo_{90}=23 vol%; Mokoia: Fo_{100}=19.3 vol% and Fo_{90}=13.3 vol%; Howard et al., 2010), while the Allende-like population lack hydrated minerals altogether and do not contain pure fayalite (Weisberg et al., 2006; MacPhearson & Krot, 2014). Further differences are observed in the abundance and speciation of secondary minerals formed by metasomatic alteration (MacPhearson & Krot, 2014). Fe-rich olivine and diopside-hedenbergite are found in all CVs. CV_{ox} and CV_{red} groups can be distinguished as CV_{ox} (especially the Allende-like members) contain nepheline, sodalite, andradite, magnetite and Fe-Ni-sulfides, whereas, these minerals are rare or absent in the CV_{red} group that instead contain kirschteinite (MacPhearson & Krot, 2014).

These distinct petrographies require different alteration histories operating on the theoretical pristine CV material. The oxidised subgroup is enriched in alkali elements and Fe-rich silicates, attesting to Fe-alkali-halogen metasomatism (Krot et al., 1995; 1998). However, the formation of fayalite remains unresolved. Different processes have been invoked such as: alteration of low-Ca pyroxene into fayalitic olivine (Housley and Cirlin, 1983), hydrothermal growth of fayalite (Krot et al., 2004) or the formation of fayalite through dehydration of phyllosilicates (Brearley, 1999). At present, the most accredited mechanism of formation of fayalite is development during thermal metamorphism by growth from an amorphous precursor phase whilst in the presence of aqueous fluids (Abreu and Brearley, 2011). Thermodynamic constraints on the formation of fayalite were delineated by Zolotov et al. (2006) who suggested that the presence of Ca-Fe-silicates (fayalite, nepheline, sodalite, diopside-hedenbergite, andradite, grossular, kirschteinite and phyllosilicates) are clear evidence of alteration from primary minerals held inside CAIs (i.e. melilite, anorthite, Al-Ti-diopside, hibonite, spinel and perovskite) (Krot et al., 1995) with dissolution of anorthite and albite in chondrule mesostasis releasing CaO and SiO_2 for secondary mineral growth (Krot et al., 1995).

Among micrometeorite collections only two particles have previously been recognized as CV-like (Genge, 2010 and van Ginneken et al., 2012), although neither were the subject of a detailed investigation into their parent body processing, a task that we discuss in this work with a more detailed characterisation of the CV-like TAM5.29 particle. Furthermore, the classification of these samples as a CV-like reveals some issues. The particle described by van Ginneken et al. (2012) contains wüstite instead of Fe-Ni metal and the magnetite composition does not fall in the CV magnetite field. On the other hand, the sample described by Genge (2010) shows olivines with rounded morphologies and a high density of crystal defects, which are not typical characteristics of CVs. For this reason, van Ginneken et al. (2012) and Genge (2010) also suggested an affinity with CO chondrites. In addition TAM5.29 has andradite inclusions, diopside crystals and oriented petrofabric

of olivine that were not detected in the two other CV-like particles described by Genge (2010) and van Ginneken et al. (2012), making TAM5.29 different and unique with an enhanced metasomatic history and with an undoubted metamorphosed CV-like mineralogy.

Micrometeorites from anhydrous CC groups are relatively rare, although up to the 50% of the incoming micrometeorite flux have oxygen isotopic compositions related to the CO/CV/CK anhydrous supergroup (Suavet et al., 2010). Thus, the characterisation of unique micrometeorites and those derived from rare parent bodies is crucial for our collective understanding of the near-Earth dust complex and the diversity of the asteroid belt.

Here we provide a detailed characterisation of the third CV-like cosmic dust particle with unique mineralogy and fabric, expanding knowledge in the compositional range of micrometeorites as well as investigating the thermal metamorphism and hydrothermal history of the CV parent body-(ies). Furthermore, given that micrometeorites originate from the asteroid belt (Genge et al., 2008; van Ginneken et al., 2012) and cometary sources (Noguchi et al., 2015), the study of this sample can be a useful support to recent and upcoming space missions to C-type asteroids (e.g. NASA-Dawn mission at [1] Ceres, Hayabusa 2 at [162173] Ryugu, Osiris-Rex at [101955] Bennu) giving possible insights into the surface and subsurface composition and geological events. In particular, TAM5.29 with its particular metasomatic history adds knowledge on aqueous alteration and hydrothermalism, that are known to characterise C-type asteroids, and the relative products: secondary mineral formation in particular hydrous minerals like phyllosilicates, the formation of opaque phases and post accretion processing of organic matter, especially aliphatic and aromatic hydrocarbons.

2. Methods

2.1 Sample collection

TAM5.29 (~300 µm x ~600 µm) was recovered from Frontier Mountain (72°59'S–160°20'E; at ~2800m above sea level and ~600m above the local icesheet surface), within Victoria Land, Antarctica. TAM5.29 was collected by the Italian Programma Nazionale delle Ricerche in Antartide (PNRA) during the 2003 expedition (Folco et al., 2008). Frontier Mountain consists of igneous rocks belonging to the Granite Harbour Igneous Complex. The top of the mountain is characterised by flat-glacially eroded surfaces, created by an overriding icesheet in the past (Folco et al., 2008). On these flat surfaces numerous joints and weathering pits are found. These are filled with loose fine-grained bedrock detritus in which thousands of micrometeorites accumulated during the last ~1-2 million years along with a relatively small component of background terrestrial sediment (Folco et al., 2008).

2.2 Petrography and major element analysis

Particle TAM5.29 was embedded in epoxy resin, sectioned and polished. The resulting thick section was used for whole-section petrographic analysis using a field-emission scanning electron microscope (ESEM-FEG-STEM FEI Quanta 450), equipped with microanalytical EDS (Energy Dispersive Spectrometry) Bruker, QUANTAX 400 XFlash Detector 6|10, which has a 129 eV spectral resolution and an intermediate size 10 mm^2 detector plate, capable of rapid-data collection and semi-quantitative results at the Centro Interdipartimentale di Scienza e Ingegneria dei Materali (CISIM), University of Pisa. All analyses were performed under high-vacuum and at a fixed working distance of 10.0 mm (the optimal sample-to-pole-piece distance to maximise X-ray counts at the EDS detector on this instrument). Operating conditions are standardized for our lab and use an electron beam accelerating voltage of 15 kV and an unmonitored beam current. Spectra were acquired with an acquisition time of 30s maintaining a dead time of approximately 10%. EDS data reported are

therefore uncalibrated and standard-less. Weight totals were determined using the Bruker's "*interactive oxides*" and are quoted as weight normalized values in Table S1-S2. Elemental detection limits for this instrument are on the order of 0.2-0.5 wt%.

Mineral phases were identified by Raman measurements at the Department of Geosciences, University of Padova, using a Thermo Scientific™ DXR™ Raman Microscope using a 532 nm laser excitation source. Analyses were performed using a 50x and 100x long working distance objective with ~2.5 cm^{-1} spectral resolution, ~1 µm spatial resolution and 25 µm pinhole operating at a minimum of 1 mW to a maximum of 5 mW of power. Low power (1 to 5 mW) coupled with short exposure times of 3-4 s was essential to avoid damage to minerals and carbonaceous phases. To minimise noise, each spectrum was acquired 10 to 15 times. Spectra were recorded in the frequency range from 100 to 3500 cm^{-1}. Spectral fitting was carried out using the Thermo Scientific™ OMNIC™ Spectra Software. Rectangular areas were analysed with the Raman *point-by-point* mapping technique – again each spectrum in the map was collected 10-15 times using an exposure time of 3 to 4 s and spectra were obtained from a grid of points spaced 2 µm along X axis and 2 µm along Y axis.

EBSD analysis was performed on a CamScan 2500 SEM (Department of Geosciences, University of Padova) equipped with a LaB6 source, a NordlysNano EBSD detector of Oxford Instruments and Channel 5.12 EBSD acquisition- and post-processing software. The sample was for one-hour Syton polished to remove surface damage related to conventional diamond polishing, and was then carbon coated (few nanometers of thickness) to improve conductivity. Operation conditions were 25 mm working distance, 15 kV beam acceleration and 10 nA probe current. Considered the small grain size of the olivine crystals, for EBSD mapping in automated mode a 0.1 µm step-size in X and Y directions was applied during acquisition of a 600 x 400 data grid. EBSD does not discriminate between solid-solutions of olivine, garnet and Clinopyroxene (Cpx), therefore forsterite and diopside reflector files of the HKL database were used to index olivine and Cpx, whereas andradite of the American Mineralogist Crystal Structure Database (Downs and Hall-Wallace, 2003) was used to index andradite. Indexing of the EBSD-patterns was accepted when at least 6 Kikuchi bands were detected. EBSD data were processed using the Oxford Instruments HKL software package Channel 5.12, generating crystallographic orientation maps, band contrast maps, phase maps and pole figure plots after noise reduction. Latter was done by removing isolated misindexed data points using a wildspike correction, whereas all non-indexed points were infilled to a six nearest-neighbour crystallographic orientation by extrapolation. In the Channel 5.12 software package grain detection in EBSD maps is based on crystallographic orientation, using a misorientation angle of at least 10° between two adjacent pixels to identify grain boundaries. Grain orientation data from the entire map were plotted onto lower hemisphere equal area projections as one point per grain to avoid grain size related bias during contouring.

We determined bulk mineralogy through µXRD diffraction methods, using a Rigaku Rapid II micro-diffraction system, equipped with a 2D curved imaging plate detector, at the Department of Earth Science, The Natural History Museum in London. This was employed to collect in-plane diffraction pattern data from the TAM5.29 sample. A Cu X-ray source with an incident beam monochromator provided K filtered Cu-Kα radiation (1.5418 Å). This was collimated by a pinhole system to a beam spot of 100µm. Analysis ran for 10 hours, after which the 2D diffraction image was converted to a 1D XRD pattern following automated removal of the background signal and integration of the Debye

rings. Data were collected on cross section samples using a constant ω angle of 16º2θ and a rotating φ axis to maximise the number of crystallites and the randomness of their orientations in the X-ray beam. Low-angle (<16°2θ) diffraction peaks could not be collected because the polished resin block, which holds the particles prevented the stage from rotating in the ω plane by <16°2θ. Peak positions in the converted 1D patterns were identified by comparison against a mineral reference database (PDF-4 database from ICDD).

EMPA spot analyses were carried out at the Department of Geosciences, University of Padova with a CAMECA SX50 instrument with 5 wavelength dispersive spectrometers. Data were acquired with a beam current of 20 nA, accelerating voltage of 20 kV, defocused beam diameter of 5 µm and we used for each element an acquisition time of 10 seconds. Amelia plagioclase, olivine, orthoclase, diopside, sphalerite (blenda), synthetic $MnTiO_3$ and Cr_2O_3 standards were used for instrumental calibration. The Pouchou-Pichoir procedure (PAP), supplied by the manufacturer, was used for raw data reduction. Detection limits (wt%) are: Na_2O=0.04; MgO=0.02; Al_2O_3=0.02; SiO_2=0.3; SO_3=0.03; K_2O=0.02; CaO=0.02; TiO_2=0.02; Cr_2O_3=0.04; MnO=0.04; FeO=0.04. We also used EMPA spot analyses to obtain the bulk composition of TAM5.29 by averaging a grid of 122 randomly spaced EMPA analyses in a specific representative area chosen on the basis of EDX maps, especially to avoid areas with major terrestrial alteration. Supporting standards-less EDS spot analyses were conducted on the FE-SEM at the University of Pisa.

Reflectance near-IR spectra were acquired at the laboratories at the IAPS-INAF (Istituto di Astrofisica e Planetologia Spaziali – Istituto Nazionale di Astrofisica). We used a microscope Micro-IR Hyperion 2000 FTIR Vertex Bruker®. The spectra were acquired in the spectral range between 1.3- 22 µm (here we focused and report only the range between 1.5 – 4.2 µm), with a MCT detector. Infragold (Labsphere®) has been used to calibrate spectral reflectace. The spectra were acquired with a spectral resolution of 2 cm^{-1} and an aperture on the sample of 150X150 µm.

3. Results

3.1 Petrography and mineral chemistry

TAM5.29 is a ~300 µm x ~600 µm sized particle with a partial magnetite rim only found along the fusion crust. The melt layer is discontinuous and the texture is similar to the fusion crust found on meteorites (Fig. 5A, Fig. S1). Voids are recognisable in the melt layer (Fig. 5A). High resolution FE-SEM imagining demonstrates that the particle is composed primarily of lath-shaped olivine crystals with widespread andradite inclusions surrounded by dark halos composed of intermixed pyroxene and jarosite, which also occur as alteration veins (Fig. 1A-B). These inclusions form lenses with an augen-like texture (Fig. 1A-B-E). A few of these lenses show a distinct asymmetrical shape (Fig. 1B). Olivine is euhedral to subhedral with dimensions from a few micrometres up to ~10 µm. Andradite appears as sub-rounded crystals 5-10 µm in size, while the diopside and jarosite surrounding these are anhedral and difficult to distinguish from one another in backscattered electron images since they are small crystals (few micrometres) finely mixed and with similar greyscales. EDS spot analyses (Table S1) reveal fayalitic olivines, with heterogeneous grain compositions, ranging from $Fa_{42.5}$ to almost pure fayalite $Fa_{92.3}$. Rare crystals of forsterite are also present (Fo_{66-71}). Similarly, pyroxenes have heterogeneous grain compositions ($Fs_{1.8-60}$ $Wo_{0.7-48}$). Owing to the small grain size, pores and limitations with the spatial resolution and the interaction volume of the electron microprobe, spot analyses on some phases suffer from beam overlap with adjacent hydrated minerals, oxides and sulphides, thus analyses shown in table S1 may reveal low weight totals (olivine 89 wt%; andradite

95 wt%). We therefore supported mineral identification with spatially resolved Raman and bulk µXRD measurements.

Raman data revealed pyroxenes to be diopside (Fig. 2) with sparsely distributed isolated enstatite grains. In figure 2 a Raman map shows the typical microtexture of this particle. Furthermore, an aggregate of spinel crystals (mean Cr/(Cr+Al)=0.003 and Fe/(Fe+Mg)=0.34 based on EMPA analyses) are present (Fig. 1C-10, Table S1-S2), these co-occur with micron-sized Fe-oxides (mainly magnetite, spinel and ferrihydrite). Only minor FeNi alloys are found (Fig. 10 and Table S2) dispersed within the matrix (Fig. 1). Raman analysis together with EDS, EMPA and EBSD suggest that a considerable portion of the olivine has been altered resulting in a mixture of fine-grained hydrated Mg-Fe-sulphur-rich minerals and minor carbonates (likely Fe-carbonates) as suggested by the 3.9 µm band in TAM5.29 IR spectra (Fig. 11), that we identify as iddingsite (see paragraph 3.3 for a more detailed description). Fine-grained phases are found as weathering films on fayalite and also scattered throughout the whole particle. Given their cryptocrystalline nature it is difficult to definitely resolve individual mineral phases, however, fibrous phyllosilicates are clearly resolved as dark haloes around andradite inclusions (Fig. 1A-B-F). Micro-XRD revealed that these fibrous phyllosilicates are mainly antigorite and saponite (Fig. 8).

The bulk composition of TAM5.29 shown in table 1 is similar to that of CCs, being within 2 orders of magnitude of CI values, and similar to other unmelted fine-grained Antarctic micrometeorites (UMM) (Fig. 3). However, TAM5.29 also demonstrates notable enrichment in Fe and depletion in Mg compared to the CCs, as also suggested by the 2.8 µm band (Fig. 11) typical of Fe-rich hydrous phases (Takir et al, 2013). The aluminium content of TAM5.29 is similar to that of CV meteorites (Table 1 and Fig. 3) and is significantly higher than other CCs – consistent with the high concentrations of refractory elements found in CV and CK chondrites. Conversely Ca and Ti are depleted compared to CVs. The spider diagram in figure 3 shows a strong enrichment in K in TAM5.29 compared to both CVs and other UMM. If we consider bulk composition of only the matrix of CVs (Table 1 and Fig. 3) we see that FeO-MgO-CaO-TiO_2 values are closer to those of TAM5.29. On the contrary Al_2O_3 and Cr_2O_3 CVs matrix values are considerably different from the values of TAM5.29, which are closer to the average CVs (considering also chondrules). Slight depletion of Na_2O in TAM5.29 compared to both CVs and CVs matrix is also found.

Carbon is also ubiquitous, Raman analyses (Fig. 2 and 6) identified characteristic “G” and “D” band peaks (located at ~1350 and ~1590 cm^{-1} respectively) and associated with disordered carbonaceous phases (Bonal et al., 2006). Poorly Graphitized Carbon (PGC) occurs as tiny inclusions of 100-200 nm in fayalite and as thin films surrounding crystals (Krot et al., 1998; Abreu and Brearley, 2011). It is interesting to note that Raman spectra of the various mineral phases (fayalite, andradite, diopside, jarosite and fine grained material) also have peaks around 2680 and 2930 cm^{-1}. These peaks are second order peaks of C but also attest to the presence of OH as well as S-H and C-H functional groups within organic molecules. Sulphur is detected in all EMPA and EDS analyses, reflecting either S in jarosite, S-bearing organics or S-rich phyllosilicates. IR reflectance spectra (Fig. 11) also show the presence of organic matter (i.e. CH compounds, aromatic and aliphatic hydrocarbons) with the 3.3 and 3.4 µm bands, the broad band between 3.6 and 3.8 µm can be instead indicative of S-H compounds. IR spectra also indicate the presence of carbonates with the 3.9 µm band (Fig. 11).

Furthermore, all EMPA and EDS analyses show low totals, indicating ubiquitous presence of OH and CH functional groups, in agreement with Raman observations.

Another important observation is a shock melt vein 136 µm in length and approximately 5 µm in thickness (Fig. 1D). This feature cross-cuts the fayalitic groundmass and either deforms or displaces the primary features (an andradite-diopside vein Fig. 1D). In addition, we observe a conjugate synthetic fracture and release band (Fig. 1D). The displacement of these features appears to show a dextral shear sense, although this interpretation remains uncertain owing to significant variations in the width of the Jarosite/diopside band on either side of the melt vein. The lower margin of the linear feature (as seen in Fig. 1D) shows an abrupt compositional contact with the host groundmass, while the upper margin is transitional over approximately 5 µm. This feature is composed of a nanocrystalline or glassy matrix with a high porosity and hosting anhedral rounded small (<2 µm) olivine crystallites and minor Fe-Ni oxides.

3.2 Preferred orientation of olivine

Figure 4 reports EBSD map data acquired on the same site shown in Fig. 1B where olivine crystals wrap around andradite-diopside/jarosite inclusions and form a foliation texture (Fig. 1B). To investigate whether the olivine crystals show a crystallographic preferred orientation (CPO), a detailed EBSD map (Fig. 4) was collected. In figure 4A, a phase map, olivine (red), andradite (green) and diopside (yellow) are shown. The dark part of the map is material that was not indexed. It is unlikely that the material between the olivine crystals has not been indexed because of potential polishing problems, since micro-Raman, SEM, EMPA and micro-XRD analysis shows the presence of fine grained alteration products (see below).

The three pole figures (Fig. 4B), lower hemisphere equal area projections, are obtained considering one point per olivine grain. This has been done to avoid a bias of the data distribution due to grain size effects. Pole figures in figure 4B show the pertinent crystallographic orientation of every single olivine crystal. In these pole figures a clear trend is recognized, with the [100] axis forming a maximum in the NW periphery, suggesting a NW-SE preferred orientation of this direction, hence orthogonally to the foliation trace. Conversely, the [010] and the [001] directions are dispersed along girdles consistent with the overall trend of the foliation trace. This implies that the [100] axis is a rotation axis, and that the differently elongated shape of the olivine crystals is the result of crystals having their [010] and [001] directions at systematically changing angles within the foliation plane.

3.3 Fine-grained material

With EDS, EMPA and Raman analyses widespread fine-grained cryptocrystalline phases are found in the TAM5.29 dust grain along with the previously described iddingsite. Raman analyses produce mixed spectra suggesting the presence of sulfides, probably related to the S-H bands as well as poorly crystalline hydrated phyllosilicates (Fig. 7). The Raman spatial resolution was 1 µm (see methods), evidence that the fine-grained material has a grain size below 1 µm. Micro-XRD data (Fig. 9-10) are in agreement with this interpretation, revealing Fe-Ni sulfides, phyllosilicates and possibly oxides and hydroxides. Carbonates are not clearly detected by Raman and micro-XRD, but their presence is inferred by the 3.9 µm band in the IR spectra (Fig. 11).

4.Discussion

4.1 TAM5.29: micrometeorite or meteorite?

TAM5.29 has a discontinuous melt layer with a texture similar to the fusion crust found on meteorites (Fig. 5A, Fig. S1). The presence of such a prominent melt layer is unusual for a micrometeorite exterior, which instead have a thin (~5-50 µm) double-layered igneous rim and magnetite rim (Genge, 2006). This could imply that TAM5.29 is a fragment of a larger meteorite.

Although meteorite fusion crusts are highly variable in composition, texture and thickness (Genge and Grady, 1998) they are commonly >1000 µm (that is 10x thicker than the crust on TAM5.29, Fig. S1). In addition, the bulk composition of CV fusion crust is also markedly different from bulk composition of TAM5.29 (Table 1). As reported by Genge and Grady (1998), they have MgO= 25.65 wt%; SiO_2= 34.5 wt%; FeO= 30.46 wt%; CaO= 2.39 wt% and Al_2O_3= 3.34 wt%. On the contrary TAM5.29 has major elements bulk composition (Table 1) of MgO= 12.6 wt%; SiO_2= 29.2 wt%; FeO= 40.1 wt%; CaO= 1.41 wt% and Al_2O_3= 4.93 wt%. Furthermore, because the melt layer on TAM5.29 is discontinuous, this requires that the particle fragmented whilst on the Earth's surface, as evidenced by the lack of fusion features on the remainder of the particle perimeter. We estimate that the pre-atmospheric particle diameter – assuming a spherical shape (a simplistic approximation given fusion crusts can show protrusions) at 1300-2000 µm, approaching the size limit for micrometeorites. Thus TAM5.29 may represent a different class of extraterrestrial material intermediate in size between micrometeorites (<2000 µm) and meteorites (~>1 cm). This size domain was previously described by Harvey and Maurette (1991), Kurat et al., (1994) and Folco and Rochette (2010) and termed "*minimeteorites*".

The hypothesis that TAM5.29 was a small particle in space is further supported by its unique petrology (chondrule-free nature and mixed metamorphic history). Owing to their unique delivery mechanism (P-R drag, operating on grains <1 cm, Gonczi et al., 1982) cosmic dust sample a more diverse collection of asteroid parent bodies than their larger meteorite counterparts. Thus, because TAM5.29 represents a new lithology, this adds to our confidence that this sample is not simply a fragment of a larger meteorite broken off during atmospheric entry but instead existed as a grain of dust in interplanetary space derived from a parent body not currently delivering meteorites to Earth and otherwise unsampled.

Finally, the preferential fragmentation of a heterogenous material, with fractures following boundaries of chondrules and CAIs may explain their absence in this minimeteorite, thereby reflecting the unrepresentative sampling (of coarse-grained features within parent body), as previously argued by Genge et al. (2008).

4.2 Terrestrial weathering

Micrometeorites from the Transantarctic Mountains often show moderate to significant terrestrial weathering. In particular, jarosite is a common product of formed in subaerial Antarctic environments (van Ginneken et al., 2016). The EDX map in figure 5C-D reveals co-occurrences of S and K, the main components of jarosite, concentrated along the particle border and in the fractures within TAM5.29. The effect of terrestrial weathering is however limited being confined to the fractures and margins. The EDX map in figure 5C reveals that high Ca concentrations correspond to andradite inclusions, unaffected by replacement. In addition, Mg and Fe-element maps (Fig. 5B) are well delineated, suggesting that these elements have not been leached by terrestrial fluids. It appears that TAM5.29 has therefore suffered limited weathering, retaining the majority of its pre-

atmospheric mineralogy unaltered. Because the melt vein displaces a dark vein of diopside + jarosite (marked in Fig. 1D), we conclude that the shock event post-dates the metasomatic event. However, it remains unclear whether iddingsite is also intersected by the melt vein or if alteration that created the iddingsite overprints the shock vein. We favour the latter option assuming that iddingsite formed by fluids released by hydrous minerals as a consequence of the pressure exerted by the impact (because olivine in TAM micrometeorites typically weathers to jarosite and not iddingsite, van Ginneken et al., 2012). Later fractures instead cut the shock melt vein creating possible localized terrestrial alteration also on the shock melt vein.

4.3 Petrogenesis – Record of hydrothermal environment on the Parent Body

The mineralogy displayed by TAM5.29, primarily composed of fayalitic olivine plus Ca-Fe rich pyroxenes, andradite, phyllosilicates and sulphides as well as the close matrix compositions demonstrate a clear affinity to the CV chondrite group. The mineralogy in TAM5.29 is, however, distinct from any currently reported CVs and also unique among reported micrometeorite studies.

TAM5.29's most common mineral – fayalite is associated with Fe-alkali-halogen metasomatism at temperatures <300°C (Krot et al., 1995-1998; Zolotov et al., 2006; MacPhearson and Krot, 2014). The preferred fayalite growing mechanism in CVs is during thermal metamorphism from an amorphous precursor phase in the presence of fluids (Abreu and Brearley 2011) and Ca-Fe-rich phases are derived from the aqueous alteration of CAIs and anorthitic-alibitic mesostasis (Krot et al., 1995).
Fe-rich olivine and diopside-hedenbergite assemblages are common in all CVs, while Ca-rich silicates (e.g. andradite) and Fe-Ni sulfides are almost absent in CV_{red}, which instead contain kirschteinite (MacPhearson and Krot, 2014). Nepheline and sodalite are typical of CV_{oxA} and absent in CV_{oxB}, which in turn contain phlogopite and saponite (MacPhearson and Krot, 2014; Krot et al., 1998). TAM5.29 is therefore consistent with the CV_{oxB} group's mineralogy, having several andradite inclusions plus phyllosilicates. This metasomatic alteration is similar to the terrestrial serpentinization-rodingitization process (Python et al., 2007; Bach and Klein, 2009). During serpentinization at temperatures <385°C clinopyroxene replaces tremolite and, at lower temperatures, below 275°C, clinopyroxene is in turn replaced by andradite (Python et al., 2007; Bach and Klein, 2009).
In summary, diopside and andradite grow at the expense of serpentine and, at lower temperatures (<275°C), andradite also replaces diopside (Python et al., 2007; Bach and Klein, 2009). Tremolite and disordered biopyriboles have been found in Allende chondrules and their presence represents a peak metamorphic temperature below 340°C (Brearley 1997). In TAM5.29 tremolite is not found. Furthermore, serpentine and diopside are small anhedral crystals that form dark haloes around andradite that appear to consume them. This provides a temperature constraint on the formation of secondary phases in TAM5.29, between 275 and 250°C, in agreement with temperatures estimated by Krot et al. (1995-1998). Krot et al. (1995-1998) based the temperature range mainly on the CV tensile strength, liquid water can exist at a maximum temperature of 310°C. This limit of 310°C is also supported by textural observations of CVs, O-isotopic composition and thermodynamic analysis (Krot et al., 1995-1998).

The bulk composition of TAM5.29 supports the Fe-alkali-halogen metasomatism hypothesis. Significant enrichment of Fe and K are observed compared to average CVs bulk composition. The enrichment in Fe is indicative of highly oxidizing conditions. However, Fe value of CVs matrix is comparable with the concentration of Fe in TAM5.29. This is probably due to the higher

concentration of Fe-oxides (i.e. magnetite and alloys) in the matrix of CVs. Instead, K is easily leached from minerals by fluids. The high concentration of K is explained with jarosite formed by terrestrial alteration (even if bulk analyses were made in areas were K enrichment due to terrestrial alteration was as low as possible based on EDX maps). It is also possible that part of the K is representative of hydrothermal fluid circulation rich in alkali elements, even if this alone cannot account for the very high K abundance in TAM5.29. In fact, localized heating on C-type bodies (e.g. Ceres) have been proposed to be due to leaching and re-deposition near the surface of long-lived radioisotopes like ^{40}K, which decays in ^{40}Ar (Castillo-Rogez et al., 2008). The Ca and Ti depletion compared to CVs is instead due to the absence of refractory inclusions in TAM5.29. However Ca and Ti concentration of TAM5.29 is higher than that in the CVs matrix. This enrichment is due to the higher concentration of Ca-rich minerals and Ti-oxides in TAM5.29, compared to the CVs matrix, formed during metasomatism. In addition, Ca depletion relative to CVs can also be related to Ca leaching that formed carbonate veins (not sampled by TAM5.29) in the parent body, a feature commonly found in terrestrial serpentinization processes (Python et al., 2007). Mg depletion in TAM5.29 is a consequence of the oxidising conditions and Fe enrichment. Na is easily depleted during aqueous alteration and TAM5.29 doesn't have nepheline and sodalite, the main carriers of Na. Al in TAM5.29 is higher than CVs and CV matrix. This high Al content is tricky to explain but is likely given by Al in the phyllosilicates derived from leached CAIs.

However, under these environmental conditions fayalite is not stable with andradite and Ni-sulfides (Krot et al., 1998; Zolotov et al., 2006; MacPhearson and Krot, 2014). Andradite is stable at higher temperatures than fayalite and the two phases can only coexist at equilibrium at T<100°C (Krot et al., 1998; MacPhearson and Krot, 2014). Temperature <100°C have also been proposed for the formation of iddingsite in the Lafayette meteorite (Treiman et al., 1993). Raman spectra and EDS analyses of TAM5.29 also show that andradite retain a certain amount of water (Fig. 2 and Table S1), thus the OH in andradite could represent a $(SiO_4)^{4-} \leftrightarrow (O^4H^4)^{4-}$ substitution reaction for which low temperature formations are also expected within a low-pressure post magmatic environment (Amthauer and Rossmann, 1998). However structural $(O_4H_4)^{4-}$ is expected to have Raman peaks at ~3560 cm^{-1} (Amthauer and Rossmann, 1998). In contrast, in TAM5.29 andradite Raman spectra show OH peaks at lower wavelengths between ~2680 and ~ 2930 cm^{-1} implying the presence of non-structural water (in addition to S-H and C-H bonds).

In support of a low temperature formation, the bulk composition of TAM5.29 shows considerable enrichment in Fe compared to all other CCs (Table 1 and Fig. 3). The majority of this Fe is held within the silicate minerals (rather than reduced Fe-Ni metal) suggesting highly oxidizing conditions at low temperatures.

Serpentinization may also occur at lower temperatures but in this case lizardite is also expected, which is not detected in TAM5.29. Instead, in TAM5.29 the presence of antigorite can only be formed by serpentinization at higher temperatures, in particular at ~310°C occurs the chrysotile breakdown to antigorite + brucite at low pressure (1 bar, which is also typical of minor bodies of the Solar System, Wunder et al., 2001). In contrast, fayalite can form over a wide range of temperatures from 30°C to 300°C with W/R (water to rock ratio) between 0.06 and 0.2 (Zolotov et al., 2006) and thus does not provide significant temperature restrictions.

Thus, the alteration assemblage in TAM5.29 must have formed across a range of temperatures, with two distinct alteration periods with distinct environmental conditions. An initial alteration regime generated the fayalite, andradite, antigorite and diopside at temperatures of ~275-250°C under oxidising conditions. While, later, at a distinctly lower temperature (<100°C), the iddingsite formed.

We conclude that fayalite-andradite-FeS-NiS assemblages derive from a retrograde metasomatism, inferred mainly by the andradite crystals consuming diopside and serpentine, at ~250°C, suggested by the mineral assemblage typical of serpentinization. Conversely, the formation of iddingsite appears to be related to an independent low-T event that will be discussed later in the discussion.

4.4 Origin of preferred orientation of olivine

The CPOs seen in the EBSD map (Fig. 4) may at a first glance resemble the terrestrial "type D" fabric of olivines recognized in simple shear experiments by Bystricky et al. (2000). Olivine "Type D" fabric refers to high stress and water-poor conditions (Michibayashi et al., 2016), and Bystricky et al. (2000) associated this fabric to upper mantle conditions, for example in regions of extensional deformation in major detachment zones near the crust-mantel boundary, or in subduction zones where hot mantle convects past the upper side of cold slabs. Such deformation regimes are inconsistent with that recorded by TAM5.29. We believe that pole figures (Fig. 4), showing a clear maximum in the [100] direction, while the [010] and [001] directions are scattered in two girdles, are describing a kind of olivine fibre texture that relate to an axially symmetric shortening regime in which the (100) plane of olivine orients orthogonally to the maximum compression direction (σ1) and relate to compaction rather than to shearing.

It is also interesting to note that the elongated olivine in TAM5.29 are generally not associated to the elongated [100] direction, but are randomly associated to the [010] and [001] directions. Further examination reveals that the longest olivine crystals show clear alignment around andradite inclusions. These preferential CPOs concentrated locally around coarse-grained inclusions were previously described in CV chondrites where olivine crystals wrap around chondrules or dark inclusions (Watt et al., 2006; Forman et al. 2017). These areas, around chondrules in CVs and around andradite crystals in TAM5.29, were probably characterised by a higher porosity compared to the rest of the matrix and thus suffered a more significant compression and pore collapse during impact. Such a scenario results in heterogeneous strain distribution with significant heat production (~575 °C) and locally high stress at the sites or pore collapse while the surrounding low-porosity matrix retains a lower degree of compaction and andradite inclusions records no compaction at all (Bland et al., 2014). The matrix therefore remains partially unaffected by the shock wave passage (Bland et al., 2014; Forman et al., 2017), while around andradite inclusions compaction is more enhanced with the creation of augen-like structures as predicted and observed in Allende by Bland et al. (2014). This process also produces a distinct heterogeneity in the CPOs (Forman et al. 2017), which is in agreement with our EBSD data.

Another intriguing fact is the dislocation of the diopside-jarosite vein in figure 1D. This vein has a dextral displacement. This kind of deformation is typically non-uniaxial and is in contrast to the theoretical uniaxial nature of the shock compaction. In support of the non-uniaxial deformation there's also the asymmetric andradite-diopside inclusion (Fig. 1B), proof of a shear stress. It seems thus that the preferred orientation of olivine has been created in the instant when the impact occurred - a moment in which stress is uniaxial. Subsequent to the initial stage of the impact, simple shear deformations form radial to the impact area (Kenkmann et al., 2014). In this second stage, deformation has been accommodated along the shock vein melt and around andradite, the two areas of TAM5.29 where weakness is higher. In particular, maximum strain occurred along the upper part of the shock vein melt where crystals were forced into the melt vein creating the transitional upper limit, the conjugate synthetic displacement and the releasing band (Fig. 1D).

Alternatively, non-impact processes may have generated the preferred orientation of olivine seen in TAM5.29. These include: sintering, sub-grain recrystallization, lithification and gravitational compaction (Forman et al., 2016-2017).

Sintering requires heating at temperatures higher than 360°C over long (>1 million years) timescales to achieve recrystallisation alignment (Gail et al., 2015). However, both the temperature and duration of heating are inconsistent with the formation conditions of TAM5.29, which require lower temperatures (~250°C) – as determined by the secondary mineral assemblage and shorter durations – as determined by Raman data and olivine crystal morphology. Likewise, the petrofabrics in TAM5.29 cannot have been formed by a plastic deformation processes such as sub-grain rotation, recrystallization and diffusion creep as these would result in significantly less elongation of olivine crystals and lower aspect ratios (Forman et al. 2017).

Petrofabrics formed by compression due to lithostatic forces cannot be ruled out, but it's less likely as also suggested by Watt et al. (2006), Format et al. (2016; 2017) and Bland et al. (2014). This is because the pressure on small protoplanets is negligible, especially on porous water-rich carbonaceous chondritic parent bodies. For example, at the centre of a 200 km diameter asteroid pressures are thought to reach a maximum of 1MPa (corresponding to a depth of a few tens of meters on Earth), far too low for lithostatic compaction (Weidenschilling and Cuzzi, 2006). Meanwhile, on larger Ceres-like bodies, pressure estimates vary between <0.2 GPa (Neumann et al., 2015) and 1220 MPa (Suttle et al., 2017). Even if sufficient pressures are possible, liberation would require an impact of an enormous magnitude, equivalent to the complete destruction of such a body. In both cases we would expect a brecciated texture of the resulting asteroid's chunks. In TAM5.29 brecciated texture is not observed. However TAM5.29 is a small fragment and does not necessarily sample an area with clasts boundaries. For this reason we cannot assume that TAM5.29 is not part of a breccia and we cannot completely rule out the possibility of lithostatic compression.

Finally, a gravitational compaction model, such as that proposed for Allende by Watt et al. (2006) may be possible. Here, a muddy outer layer of a parent body affected by sedimentary processes operating under microgravity result in the alignment of olivine. However, gravity is very low even on a Ceres-like body (Ceres gravity is ~0.28 m/s^2, around 1/35 Earth's gravity). The low gravity coupled with the chaotic [010] and [001] axis distribution of olivines in TAM5.29 (fig. 4), bring us to prefer an impact-induced compaction (Gattacceca et al., 2005; Bland et al., 2014; Forman et al., 2016-2017). Consequently, the process that most likely created the preferred orientation of olivines in TAM5.29 is impact compaction, and this is further supported by the presence of the shock melt vein within the micrometeorite.

4.5 Carbon and Poorly Graphitized Carbon (PGC)

Carbon, which is widely distributed in TAM5.29, is a powerful index of metamorphic grade. In particular the maturity of the organic matter is influenced by thermal metamorphism and can be used to establish petrologic types for individual meteorites (Bonal et al., 2006). The maturation grade of the organic matter can be determined by the study of the Raman D-band (~ 1350 cm^{-1}) and the G-band (~1580 cm^{-1}) peak parameters. In the least metamorphosed samples, the intensity of the G-band I_G is higher than the intensity of the D-band I_D, the opposite is seen in samples with higher metamorphic grade (Bonal et al., 2006). When the I_D/I_G ratio of the CV chondrites is compared to the FWHM (Full Width at Half Maximum) of the D-band (FWHD-D) two distinct groups are recognised (Fig. 6) (Bonal et al., 2006). The oxidised CVs have the highest I_D/I_G ratio (1.05 to 1.55) and lowest FWHM-D (~60 to ~100 cm^{-1}) (lower right, Fig. 6), they are known to have experienced the highest metamorphic grade (Bonal et al., 2006). In particular, these data show that Allende suffered the highest thermal metamorphism (Bonal et al., 2006). An exception to this is the meteorite Kaba,

533 which is a CV_{oxB} that lies in the upper left group (Fig. 6) showing a minor metamorphic grade typical
534 of the reduced CVs (Bonal et al., 2006). Analysis of the I_d and I_g bands from TAM5.29 (Fig. 7) shows
535 an R1 ratio (I_d/I_g)>1 and in some other cases I_d/I_g~1 (but never <1), thus TAM5.29 does not clearly
536 belong to either group. Instead, TAM5.29 values tend towards the most metamorphosed group
537 (CV_{ox}) although several values also lie in the less-metamorphosed group (Fig. 6). This is proof of the
538 highly unequilibrated nature of this micrometeorite and suggests that TAM5.29 is transitional
539 between the Kaba-like CVs and the more evolved Allende-like CVs. The reason for this unspecified
540 petrologic type are, however, not clear. It is known that within the CV parent body many different
541 environmental conditions existed from oxidising fluid-enriched locations to the reducing fluid-poor
542 localities. The TAM5.29 metamorphic grade is thus representative of a new lithology of the CV
543 parent body that experienced more oxidising conditions (resulting in significant Fe enrichment) with
544 an incomplete thermal metamorphism terminated by the impact that also created the shock melt
545 vein and preferred orientation of olivine.

546 **4.6 Origin of the fine-grained material**

547 Iddingsite is a common alteration feature that affects olivine in terrestrial rocks and is also found as
548 a native minor component in chondritic meteorites. Iddingsite forms as a weathering film and
549 represents a complex mixture of secondary hydrated silicates as well as carbonates, sulphates
550 halides and oxides. Iddingsite compositions in TAM5.29 are difficult to interpret because of their
551 very small grain size (<1 µm) and mixed phase composition, which in turn gives averaged data when
552 analysed with Raman, EDS and EMPA.
553 Lee et al. (2015) described iddingsite in the Lafayette meteorite as an alteration sequence affecting
554 olivine and augite concurrent with the formation of hydrous Fe-Mg-phyllosilicates. These newly
555 formed phyllosilicates are then partially replaced by siderite. During the growth of siderite Fe-oxides
556 also begin to form (Abreu and Brearley 2011). The alteration sequence ends with saponite and other
557 fibrous phyllosilicates replacing siderite. Tomeoka and Buseck (1985) described similar alteration
558 features in the matrix of CM chondrites formed as an intergrowth of Fe-Ni-S-O phases and
559 cronstedtite. Based on these findings we looked for possible constituent minerals of iddingsite
560 within TAM5.29.
561
562 Raman spectra of the fine-grained material of TAM5.29 (Fig. 8) show possible matches to
563 mackinawite, cronstedtite, and chukanovite (from RRUFF database). The best match among these
564 phases is the hydrated Fe-Ni sulfide mackinawite (the two peaks at 209 cm^{-1} and 279 cm^{-1} of
565 TAM5.29 are also well matched by troilite), although this lacks characteristic peaks around 525 and
566 888 cm^{-1}. Mackinawite is a poorly crystalline precipitate formed by the reaction between HS^- and Fe
567 (Lennie et al., 1997). In nature, mackinawite occurs as hydrothermal alteration product within
568 serpentinized peridotites and has also been reported in meteorites. Conditions of formation of
569 mackinawite are in agreement with the conditions of formation of TAM5.29, making this phase a
570 plausible candidate.
571 Phyllosilicates are also present. Although cronstedtite can be ruled out due to a lack of diagnostic
572 within the Raman spectra the µXRD data (Fig. 9) revealed the presence of saponite and antigorite in
573 TAM5.29. Phlogopite and clay minerals may also be present but, since diffraction data could not be
574 collected below 16°2θ and clay minerals have their main peaks in this region it is not possible to
575 obtain further details about these phases. In addition, the µXRD data also suggested the presence of
576 Fe-Ni sulfides (Fig. 9) (pentlandite in matrix olivine in Allende was reported by Brearley, 1999) as well
577 as tentative evidence of Fe-carbonates.

Collectively, these data imply that the fine-grained material in TAM5.29 is a mixture of fibrous phyllosilicates (antigorite, saponite and possibly phlogopite-cronstedtite), Fe-Ni sulfides and possibly Fe-oxy-hydroxides with a possibility of rare carbonates inferred from the 3.9 µm band in TAM5.29 IR spectra (Fig. 11). This mineralogy is in agreement with the final stage of alteration described by Lee et al. (2015) from the Lafayette meteorite, and demonstrating that TAM5.29 records a protracted episode of intense post impact aqueous alteration. Fluids involved in the formation of iddingsite may therefore derive from the partial dehydration of phyllosilicates (previously formed during metasomatism) liberated after the impact event. In this scenario iddingsite formation occurs after the interruption of metasomatism at lower temperatures and in agreement with iddingsite temperature of formation proposed by Treiman et al. (1993) (<100°C).

However, low-temperature aqueous alteration of olivine alone cannot explain the entire fine-grained mineral assemblage. Evidence also exists for the loss of CAIs. Greshake et al. (1996) reported within four CAIs, several crystals of periclase (MgO), rutile (TiO_2), calcium oxide (CaO) and corundum (Al_2O_3) inside and at grain boundaries of the constituent minerals of the inclusions. These oxides have dimensions of 50-200 nm (most of them under 100 nm), a grain size similar to the fine-grained material of TAM5.29 (<1 µm). Since Ca-rich minerals (andradite and diopside) derive from alteration of CAIs and PRCs (Plagioclase-rich chondrules, Krot et al., 2002), it is possible that TAM5.29 preserves some of these residual oxides as described by Greshake et al. (1996). CaO, Al_2O_3 and TiO_2 in fact match some of the strongest peaks in the µXRD pattern of TAM5.29 (Fig. 9). So, in addition to the previously listed minerals, we believe that residual Ca-Al-Ti oxides are present as relicts of the primary parent body CAIs and PRCs. However, there are no evidences of residual CAIs in TAM5.29. We thus infer that the residual CAIs and PRCs minerals were not in situ alteration but were mobilised by fluids circulation. In fact hibonite and spinel are two of the most resistant CAI crystals to metasomatic alteration and in strongly altered CAIs Al-Ti-diopside is replaced by ilmenite and phyllosilicates (Krot et al., 1995). Al_2O_3 may also be indicative of the presence of sericite, an alteration aggregate of fine-grained minerals such as illite, muscovite and palagonite (Al and K rich minerals) formed by hydrothermal fluids circulation. Palagonite and allophane on Earth are also alteration products volcanic glasses and water interaction. TAM5.29 had some glass content before the metasomatic event (that largely creater fayalite, see paragraph 4.3). It is possible that part of it was converted into palagonite-allophane. Allophane can also be enriched in Fe and Ti (Gerard et al., 2007). The Ti enrichment can explain the TiO_2 detection in TAM5.29. So, illite and palagonite-allophane can explain the presence of Al_2O_3 and TiO_2, but not the presence of MgO and CaO oxides. Furthermore these minerals are also K-rich, which can explain part of the high K and Al bulk concentration of TAM5.29. The fine-grained material in TAM5.29 therefore requires two distinct alteration events and derived from two different processes: Fe-Ni sulfides and oxides are residues of the metasomatic event and iddingsite components (such as saponite) are derived from weathering at lower temperature (<100°C) in presence of fluids released from hydrous minerals by an impact.

5.Conclusions

We document an unambiguous and unique minimeteorite from the CV chondrite group (a member of the CV_{OX} family), thereby expanding our collective knowledge of micrometeorite parent body diversity.

- Primary mineral phases of TAM5.29 are Fe-rich olivine, andradite and Ca-Fe-rich pyroxenes plus carbonaceous matter containing OH, S-H and C-H functional groups. Fayalite crystals grew during thermal metamorphism potentially from an amorphous precursor phase in presence of fluids.
- The fine-grained material is derived by two distinct alteration events. The metasomatic process created: Ni-Fe sulfides (e.g. mackinawite), Mg-Ca-Al-Ti oxides partly derived by residual CAIs constituents mobilised by fluids and partly derived by illite-palagonite-allophane derived by aqueous alteration. Low temperature alteration created: Mg-Fe-phyllosilicates (saponite and possibly phlogopite), possibly minor Fe carbonates and FeO-OH.
- TAM5.29 mineralogy lies in between the CV_{oxA} and CV_{oxB}. CV_{oxA} are rich in andradite, magnetite and FeNiS like TAM5.29 but lacks of high abundances of hydrated minerals, common in TAM5.29. Conversely CV_{oxB} are rich in hydrated phyllosilicates but contains almost pure fayalite not found in TAM5.29. TAM5.29 retains a mineralogical assemblage that might be a link between the CV_{oxA} and CV_{oxB}.
- TAM5.29 retains a mineralogy dominated by thermal metamorphism products formed at ~275-250°C within the presence of Fe-alkali-halogens-rich fluids and under highly oxidizing conditions resulting in significant Fe enrichment.
- This may represent a newly described alteration environment on the CV parent body, similar to the conditions recorded by Allende-Axtell-Mokoia-Kaba etc. but with differences. These differences are: higher oxidizing conditions, heterogeneous thermal metamorphism that shows different degrees of alteration within only one micrometeorite and a different secondary alteration history enabled by a particular impact history.
- This is the proof of an even more heterogeneous CV parent body(-ies) thus adding a unique sample to the known CV lithologies.

In conclusion, the hypothesis of formation of the TAM5.29 micrometeorite may be divided in three main stages:

- Stage one: metasomatism at ~275-250°C with Fe-alkali-halogens-rich fluids occurred on the parent body.
- Stage two: the particle was involved in an impact that terminated the metamorphic event resulting in a strongly unequilibrated composition with cryptocrystalline and amorphous phases and generating a preferred orientation olivine petrofabric.
- Stage three: characterised by the formation of iddingsite at lower temperatures, possibly from fluid released by hydrated minerals during the impact.

Acknowledgements

We thank Stefania Stefani for the access and support to the spectroscopy laboratory at the INAF Rome. We are also grateful to Randa Anis Ishak and to Fabrizio Campanale for the support with the FE-SEM-EDS analyses as well as to Raul Carampin for the technical support with the EMPA analyses. Special thank to Sofia Genovesi, undergraduated student at the University of Bologna, who helped us acquiring bulk composition during her internship at the University of Padua. We also want to thank Mathias van Ginneken who prepared the resin block containing the MM samples. This work was supported by MIUR grants: Meteoriti Antartiche (PI# PNRA16_00029) and Cosmic Dust (PI# PRIN2015_20158W4JZ7).

References

1. Abreu N. M. & Brearley A. J. 2011. Deciphering the nebular and asteroidal record of silicates and organic material in the matrix of the reduced CV3 chondrite Vigarano. Meteoritics & Planetary Science, 46:252-274.
2. Amthauer G. & Rossman G. R. 1998. The hydrous component in andradite garnet. *American Mineralogist*, *83*(7-8):835-840.
3. Bach W. & Klein F. 2009. The petrology of seafloor rodingites: insights from geochemical reaction path modeling. *Lithos*, *112*(1-2):103-117.
4. Bland P.A., Collins G.S., Davidson T.M., Abreu N.M., Ciesla F.J., Muxworthy A.R. and Moore J. 2014. Pressure-temperature evolution of primordial Solar System solids during impact-induced compaction. Nature Communications, 5:5451.
5. Bonal L., Quirico E., Bourot-Denise M. & Montagnac G. 2006. Determination of the petrologic type of CV3 chondrites by Raman spectroscopy of included organic matter. Geochimica et Cosmochimica Acta, 70:1849-1863.
6. Brearley A.J. 1999. Origin of graphitic carbon and pentlandite in matrix olivines in the Allende meteorite. Science, 285:1380-1382.
7. Brearley, A. J., & Jones, R. H. 1998. Planetary materials. *Reviews in Mineralogy and Geochemistry*, *36*, 3-1.
8. Bystricky M, Kunze K, Burlini M., & Burg J.-P., 2000. High Shear Strain of Olivine Aggregates: Rheological and Seismic Consequences. Scienze, 290, 1564-1567.
9. Castillo-Rogez J. C., Matson D. L., Kargel J. S., Vance S. D. & Johnson T. V. 2008. Role of hydrothermal geochemistry in the geophysical evolution of icy bodies. In *Lunar and Planetary Science Conference* (Vol. 39, p. 2461).
10. Carporzen L., Weiss B.P., Elkins-Tanton L.T., Shuster D.L., Ebel D. and Gattacceca J. 2011. Magnetic evidence for a partially differentiated carbonaceous chondrite parent body. Proceedings of the National Academy of Sciences, 108:6386-6389, doi:10.1073/pnas.1017165108.
11. .Downs R.T, & Hall-Wallace M. 2003. The American Mineralogist Crystal Structure Database. American Mineralogist 88, 247-250. (pdf file)
12. Elkins-Tanton L.T., Weiss B.P. and Zuber M.T. 2011. Chondrites as samples of differentiated planetesimals. Earth and Planetary Science Letters, 305:1-10, doi:10.1016/j.epsl.2014.11.019.
13. Folco L. and Rochette P. 2010. Minimeteorites from the Transantarctic Mountains. Meteoritics and Planetary Science Supplement, 73.
14. Folco L., Rochette P., Perchiazzi N., D'Orazio M., Laurenzi M.A. & Tiepolo, M. 2008. Microtektites from Victoria land transantarctic mountains. Geology, 36.291-294.
15. Forman L. V., Bland P. A., Timms N. E., Collins G. S., Davison T. M., Ciesla F. J., Benedix G.K., Daly L., Trimby P.W., Yang L. & Ringer, S. P. 2016. Hidden secrets of deformation: Impact-induced compaction within a CV chondrite. *Earth and Planetary Science Letters*, *452*, 133-145.
16. Forman L. V., Bland P. A., Timms N. E., Daly L., Benedix G. K., Trimby P. W., Collins G.S. & Davison, T. M. 2017. Defining the mechanism for compaction of the CV chondrite parent body. *Geology*, *45*:559-562.
17. Gail H. P., Henke S. & Trieloff M. 2015. Thermal evolution and sintering of chondritic planetesimals-II. Improved treatment of the compaction process. Astronomy & Astrophysics, 576, A60.
18. Gattacceca J., Rochette P., Denise M., Consolmagno G. & Folco L. 2005. An impact origin for the foliation of chondrites. *Earth and Planetary Science Letters*, *234*(3-4), 351-368.
19. Genge M. J. 2006. Igneous rims on micrometeorites. *Geochimica et Cosmochimica Acta*, *70*(10):2603-2621.
20. Genge M.J. 2010. A Primitive Micrometeorite with Affinities to CV3 Chondrite Matrix. Meteoritics and Planetary Science Supplement, 73.

21. Genge M.J. and Grady M.M. 1998. The fusion crusts of stony meteorites: Implications for the atmospheric reprocessing of extraterrestrial materials. Meteoritics & Planetary Science, 34:341-356, doi:10.1111/j.1945-5100.1999.tb01344.x.
22. Genge M. J., Grady M. M. & Hutchison R. 1997. The textures and compositions of fine-grained Antarctic micrometeorites: Implications for comparisons with meteorites. *Geochimica et Cosmochimica Acta*, *61*(23):5149-5162.
23. Genge M. J., Engrand C., Gounelle M. & Taylor S., 2008. The classification of micrometeorites. *Meteoritics & Planetary Science*, *43*:497-515.
24. Gérard M., Caquineau S., Pinheiro J. & Stoops G. 2007. Weathering and allophane neoformation in soils developed on volcanic ash in the Azores. *European journal of soil science*, *58*(2), 496-515.
25. Greshake A., Bischoff A., Putnis A. & Palme H. 1996. Corundum, rutile, periclase, and CaO in Ca, Al-rich inclusions from carbonaceous chondrites. Science, 272(5266):1316-1318.
26. Gonczi, R., Froeschlé, C., & Froeschle, C. 1982. Poynting-Robertson drag and orbital resonance. *Icarus*, *51*(3), 633-654.
27. Harvey R. P. & Maurette M. 1991. The origin and significance of cosmic dust from the Walcott Névé, Antarctica. In *Lunar and Planetary Science Conference Proceedings* (Vol. 21, pp. 569-578).
28. Housley R.M. and Cirlin E.H. 1983. On the alteration of Allende Chondrules and the formation of matrix. In Chondrules and Their Origins (ed. E. D. King), pp. 145-161. Lunar and Planetary Institute, Houston, Texas, USA.
29. Howard K. T., Benedix G. K., Bland P. A. & Cressey G. 2010. Modal mineralogy of CV3 chondrites by X-ray diffraction (PSD-XRD). *Geochimica et Cosmochimica Acta*, *74*(17), 5084-5097.
30. Jones, R.H. 2012. Petrographic constraints on the diversity of chondrule reservoirs in the protoplanetary disk. Meteoritics and Planetary Science, 47:1176-1190, doi:10.1111/j.1945-5100.2011.01327.x.
31. Jung H., Katayama I., Jiang Z., Hiraga T. & Karato S. I. 2006. Effect of water and stress on the lattice-preferred orientation of olivine. Tectonophysics, 421:1-22.
32. Kenkmann T., Poelchau M. H. & Wulf G. 2014. Structural geology of impact craters. *Journal of Structural Geology*, *62*:156-182.
33. King, T. V., & King, E. A. 1981. Accretionary dark rims in unequilibrated chondrites. *Icarus*, *48*(3), 460-472.
34. Krot A.N., Scott E.R.D. and Zolensky M.E. 1995. Mineralogical and chemical modification of components in CV3 chondrites: nebular or asteroidal processing?. Meteoritics, 30:748-775.
35. Krot A.N., Petaev M.I., Scott E.R.D., Choi B-.G., Zolensky M.E. and Keil K. 1998. Progressive alteration in CV3 chondrites: more evidence for asteroidal alteration. Meteoritics & Planetary Science, 33:1065-1085.
36. Krot A. N., Hutcheon I. D. & Keil K. 2002. Plagioclase-rich chondrules in the reduced CV chondrites: Evidence for complex formation history and genetic links between calcium-aluminum-rich inclusions and ferromagnesian chondrules. *Meteoritics & Planetary Science*, *37*(2):155-182.
37. Krot A.N., Petaev M.I. and Bland P.A. 2004. Multiple formation mechanism of ferrous olivine in CV carbonaceous chondrites during fluid-assisted metamorphism. Antarctic Meteorite Research, 17:153-171.
38. Kurat G., Koeberl C., Presper T., Brandstätter F. & Maurette M. 1994. Petrology and geochemistry of Antarctic micrometeorites. *Geochimica et Cosmochimica Acta*, *58*(18), 3879-3904.
39. Lee M. R., Tomkinson T., Hallis L. J. & Mark D. F. 2015. Formation of iddingsite veins in the Martian crust by centripetal replacement of olivine: Evidence from the nakhlite meteorite Lafayette. Geochimica et Cosmochimica Acta, 154:49-65.
40. Lennie A. R., Redfern S. A., Champness P. E., Stoddart C. P., Schofield P. F. & Vaughan D. J. 1997. Transformation of mackinawite to greigite; an in situ X-ray powder diffraction and transmission electron microscope study. *American Mineralogist*, *82*(3-4):302-309.

41. MacPherson G.J. and Krot A.N. 2014. The formation of Ca-Fe-Rich silicates in reduced and oxidised CV chondrites: the roles of impact-modified porosity and permeability, and heterogeneous distribution of water ices. Meteoritics & Planetary Science, 49:1250-1270, doi: 10.1111/maps.12316.
42. Mauler A., Bystricky M., Kunze K. & Mackwell S. 2000. Microstructures and lattice preferred orientations in experimentally deformed clinopyroxene aggregates. *Journal of Structural Geology*, *22*(11-12):1633-1648.
43. McSween Jr, H.Y. 1977. Petrographic variations among carbonaceous chondrites of the Vigarano type. Geochimica et Cosmochimica Acta, 41:1777-1790, doi:10.1016/0016-7037(77)90210-1.
44. Michibayashi, K., Mainprice, D., Fujii, A., Uehara, S., Shinkai, Y., Kondo, Y., Ohara, Y., Ishii, T., fryer P., Bloomer, S.H., Ishiwatari, A., Hawkins, J.W. & Ji, S. 2016. Natural olivine crystal-fabrics in the western Pacific convergence region: A new method to identify fabric type. *Earth and Planetary Science Letters*, *443*, 70-80.
45. Neumann W., Breuer D. & Spohn T. 2015. Modelling the internal structure of Ceres: coupling of accretion with compaction by creep and implications for the water-rock differentiation. Astronomy & Astrophysics, 584, A117.
46. Noguchi T., Ohashi N., Tsujimoto S., Mitsunari T., Bradley J. P., Nakamura T., Tho S., Stephan T., Iwata N. & Imae N. 2015. Cometary dust in Antarctic ice and snow: Past and present chondritic porous micrometeorites preserved on the Earth's surface. Earth and Planetary Science Letters, 410:1-11.
47. Python M., Ceuleneer G., Ishida Y., Barrat J. A. & Arai S. 2007. Oman diopsidites: a new lithology diagnostic of very high temperature hydrothermal circulation in mantle peridotite below oceanic spreading centres. *Earth and Planetary Science Letters*, *255*(3-4):289-305.
48. Scott E.R., Keil K. and Stoeffler D. 1992. Shock metamorphism of carbonaceous chondrites. Geochimica et Cosmochimica Acta, 56:4281-4293, doi:10.1016/0016-7037(92)90268-N.
49. Suavet C., Alexandre A., Franchi I. A., Gattacceca J., Sonzogni C., Greenwood R. C., Folco L. & Rochette P. 2010. Identification of the parent bodies of micrometeorites with high-precision oxygen isotope ratios. Earth and Planetary Science Letters, 293:313-320.
50. Suttle M.D., Genge M.J. and Russell S.S. 2017. Shock fabrics in fine-grained micrometeorites. Meteoritics & Planetary Science, 52:2258-2274, doi:10.1111/maps.12927
51. Takir D. & Emery J. P. 2012. Outer main belt asteroids: Identification and distribution of four 3-μm spectral groups. Icarus, 219(2):641-654.
52. Takir, D., Emery, J. P., Mcsween Jr, H. Y., Hibbitts, C. A., Clark, R. N., Pearson, N., & Wang, A. 2013. Nature and degree of aqueous alteration in CM and CI carbonaceous chondrites. *Meteoritics & Planetary Science*, *48*(9), 1618-1637.
53. Tomeoka K. & Buseck P. R. 1985. Indicators of aqueous alteration in CM carbonaceous chondrites: Microtextures of a layered mineral containing Fe, S, O and Ni. Geochimica et Cosmochimica Acta, 49(10):2149-2163.
54. Tomeoka, K., and Tanimura, I., 2000. Phyllosilicate-rich chondrule rims in the Vigarano CV3 chondrite: Evidence for parent-body processes. Geochimica et Cosmochimica Acta, 64:1971-1988.
55. Tomeoka K. and Ohnishi I. 2010. Indicators of parent-body processes: hydrated chondrules and fine-grained rims in the Mokoia CV3 carbonaceous chondrite. Geochimica et Cosmochimica Acta, 74:4438-4453, doi:10.1016/j.gca.2010.04.058.
56. Treiman A. H., Barrett R. A. & Gooding J. L., 1993. Preterrestrial aqueous alteration of the Lafayette (SNC) meteorite. *Meteoritics*, *28*:86-97.
57. van Ginneken M., Folco L., Cordier C. and Rochette P. 2012. Chondritic micrometeorites from the Transantarctic Mountains. Meteoritics & Planetary Science, 47:228-247, doi:10.1111/j.1945-5100.2011.01322.x.
58. van Ginneken M., Genge M.J., Folco L. and Harvey R.P. 2016. The weathering of micrometeorites from the Transantarctic Mountains. Geochimica et Cosmochimica Acta, 179:1-31, doi:10.1016/j.gca.2015.11.045.

59. Warren P.H. 2011. Stable-isotopic anomalies and the accretionary assemblage of the Earth and Mars: A subordinate role for carbonaceous chondrites. Earth and Planetary Science Letters, 311:93-100, doi:10.1016/j.epsl.2011.08.047.
60. Watt L. E., Bland P. A., Prior D. J. & Russell S. S. 2006. Fabric analysis of Allende matrix using EBSD. *Meteoritics & Planetary Science*, *41*(7):989-1001.
61. Weidenschilling S. J. & Cuzzi J. N. 2006. Accretion dynamics and timescales: Relation to chondrites. Meteorites and the early solar system II, 1, 473-485.
62. Weisberg M.K., McCoy T.J. and Krot A.N. 2006. Systematics and evaluation of meteorite classification. In Meteorites and the Early Solar System II, D. S. Lauretta and H. Y. McSween Jr. (eds.), University of Arizona Press, Tucson, 943:19-52.
63. Weiss B.P. and Elkins-Tanton L.T. 2013. Differentiated planetesimals and the parent bodies chondrites. Annual review of Earth and Planetary Science, 41:529-560, 10.1146/annurev-earth-040610-133520.
64. Wunder B., Wirth R. & Gottschalk M. 2001. Antigorite pressure and temperature dependence of polysomatism and water content. *European Journal of Mineralogy*, *13*(3):485-496.
65. Zolotov M. Y., Mironenko M. V. & Shock E. L. 2006. Thermodynamic constraints on fayalite formation on parent bodies of chondrites. Meteoritics & Planetary Science, 41:1775-1796.

842 Table 1. Bulk composition obtained from 122 random EMPA analyses (oxide wt%) of TAM5.29
843 micrometeorite compared with bulk composition of carbonaceous chondrites and average
844 composition of unmelted fine-grained Antarctic micrometeorites (UMMs).

	TAM5.29		CV*	CM*	CO*	CI*	CK*	CR*	UMMs**	CV matrix
	Mean	σ	Mean	Mean	Mean	Mean	Mean	Mean	Mean	Mean
Na_2O	0.26	0.18	0.46	0.48	0.47	1.13	0.42	0.31	0.44	0.46
MgO	12.6	3.23	23.3	20.9	23.9	19.1	24.4	17.4	16.8	18.8
Al_2O_3	4.93	8.34	4.02	2.55	2.98	2.02	2.98	2.31	4.28	2.49
SiO_2	29.2	4.95	33.2	30.1	33.9	27.3	34.2	31.9	33.9	28.6
P_2O_5	n.d.	-	0.28	0.27	0.25	0.28	0.25	0.29	0.40	n.d.
SO_3	2.17	2.22	3.96	8.6	2.34	17.9	2.9	2.7	1.9	3.29
K_2O	0.28	0.65	0.04	0.06	0.06	0.11	0.04	0.04	0.13	0.02
CaO	1.41	2.58	3.50	1.96	2.26	1.71	2.39	1.91	0.72	0.85
TiO_2	0.12	0.27	0.24	0.13	0.13	0.10	0.18	0.10	0.11	0.07
Cr_2O_3	0.53	0.42	0.50	0.47	0.52	0.42	0.53	0.53	0.49	0.36
MnO	0.15	0.05	0.19	0.24	0.23	0.28	0.18	0.22	0.23	0.23
FeO	40.1	6.61	28.9	29.5	31.3	28.5	30.3	30.4	29.6	37.6
NiO	n.d.	-	1.37	1.19	1.66	1.13	1.44	1.72	0.37	1.65
TOT.	91.8		100	96.5	99.9	100	100.2	89.9	89.4	94.5

845 n.d.: Not Determined
846 * from MetBase.
847 ** from Genge et al., 1997.

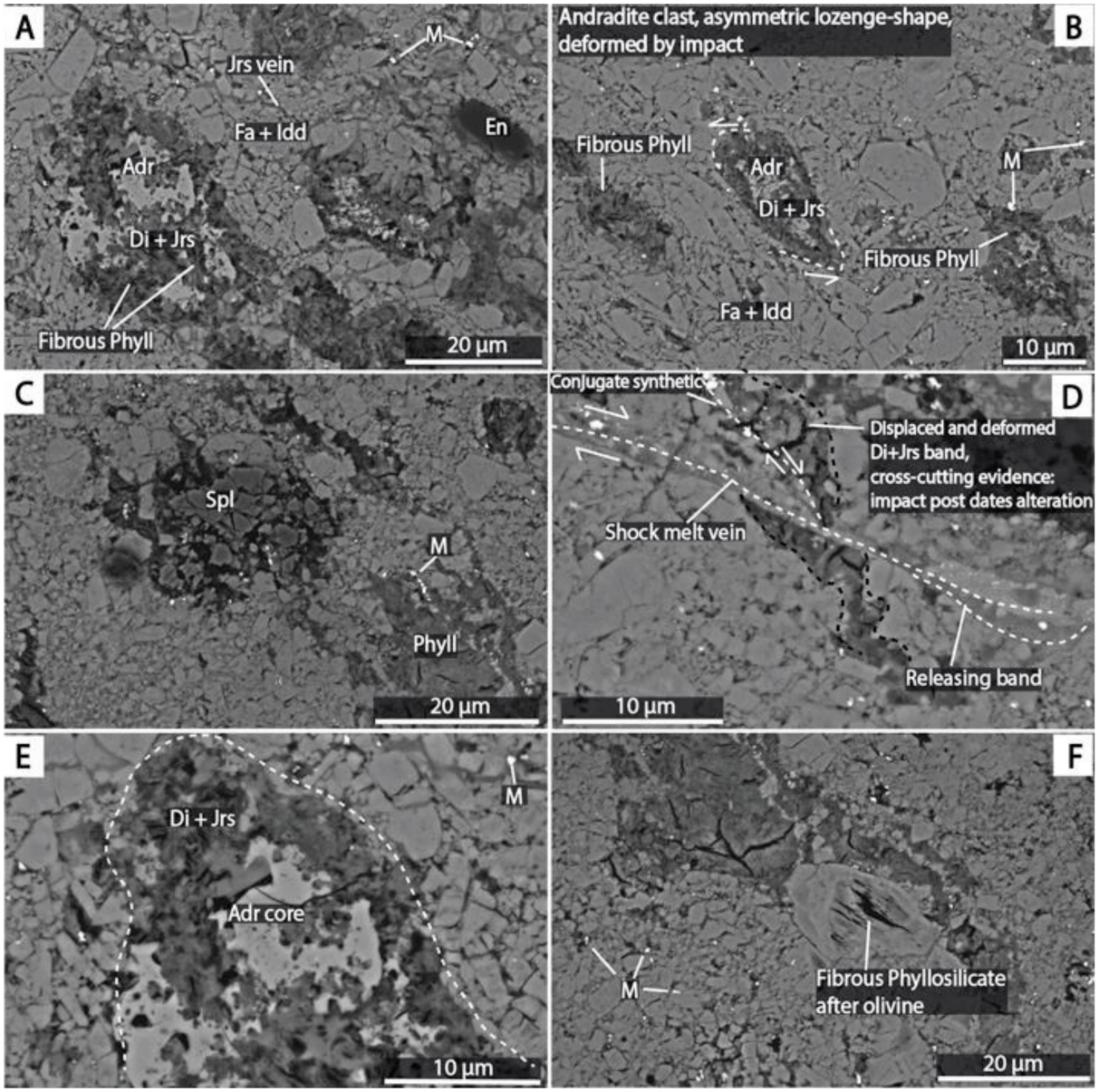

Fig.1. TAM5.29 FE-SEM BSE images. A-B-E) Typical mineral association of TAM5.29 with andradite surround by diopside, jarosite and fibrous phyllosilicates in a matrix made of iron rich olivine alterated in iddingsite. Many metal grains can be seen. C) Isolated spinel crystals. D) shock melt vein that sharply cuts other crystals. F) Fibrous phyllosilicates. Fa=fayalite, Di=diopside, Adr=andradite, Jrs=jarosite, En=enstatite, Phyll=phyllosilicate, M=metal alloys-oxides, Spl=spinel, Idd=iddingsite.

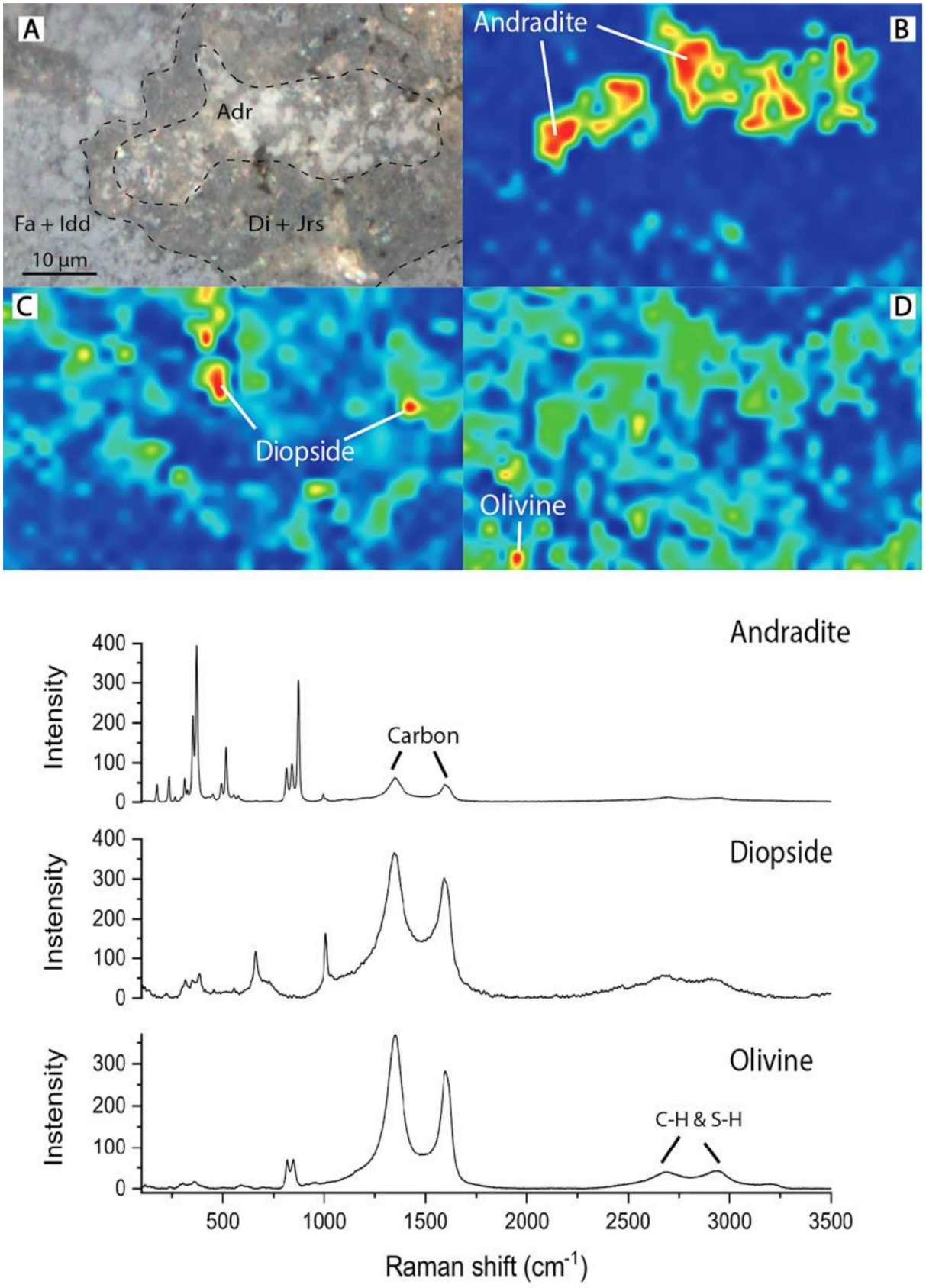

Fig. 2. Raman map showing a typical assemblage of TAM5.29 (A) consisting of andradite inclusions (B) surrounded by dark halos composed of intermixed pyroxene and jarosite (C), immersed in an olivine matrix (D). Abbreviations as in figure 1.

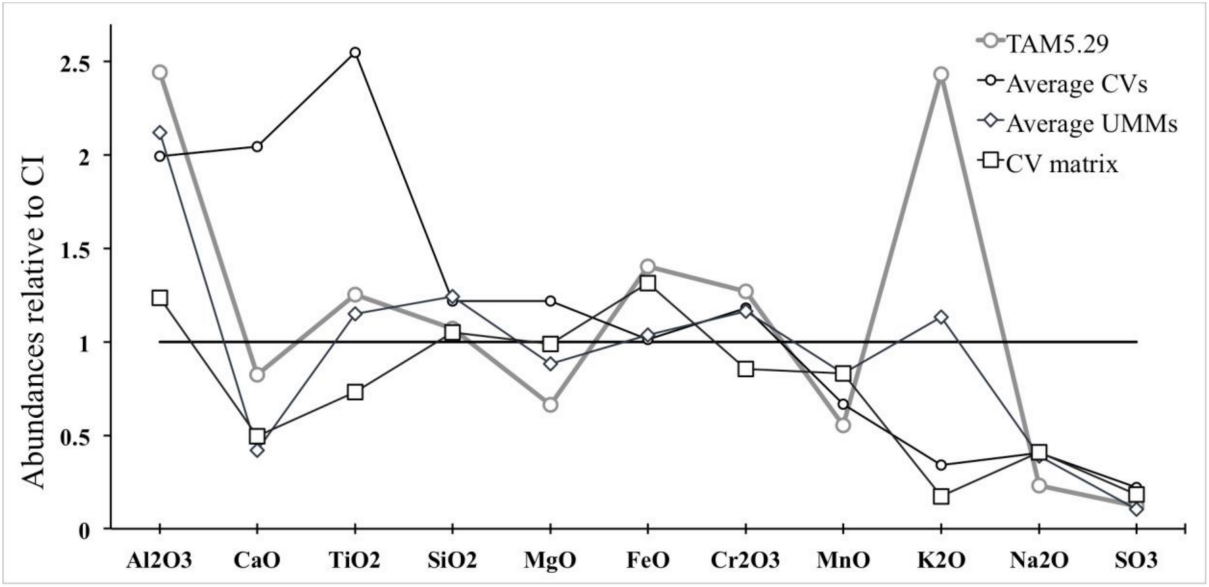

Fig. 3. Bulk composition of TAM5.29, average CVs (data from METDB database), average CV matrix and average Unmelted fine-grained Antarctic micrometeorites (UMMs) (data from Genge et al., 1997) relative to the CI chondrites composition.

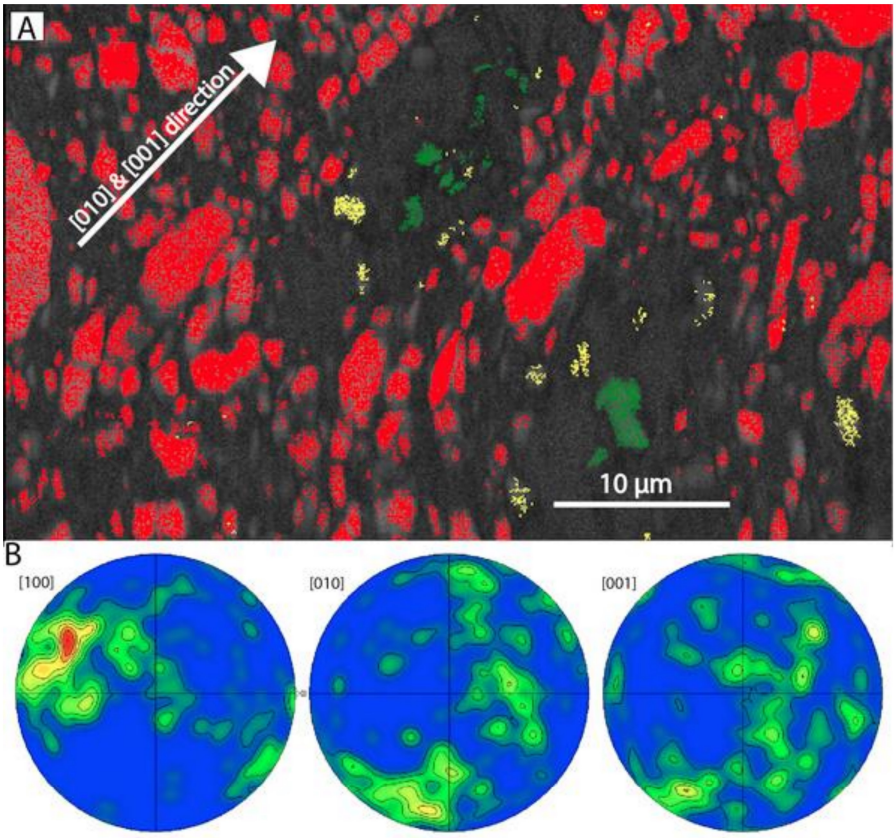

Fig. 4. A) EBSD phase map of the same area in fig. 1B with relative pole figures of olivine (panel B, one point per grain). Red=olivine, green=andradite, yellow=diopside and black-grey area are fine grained undetected material.

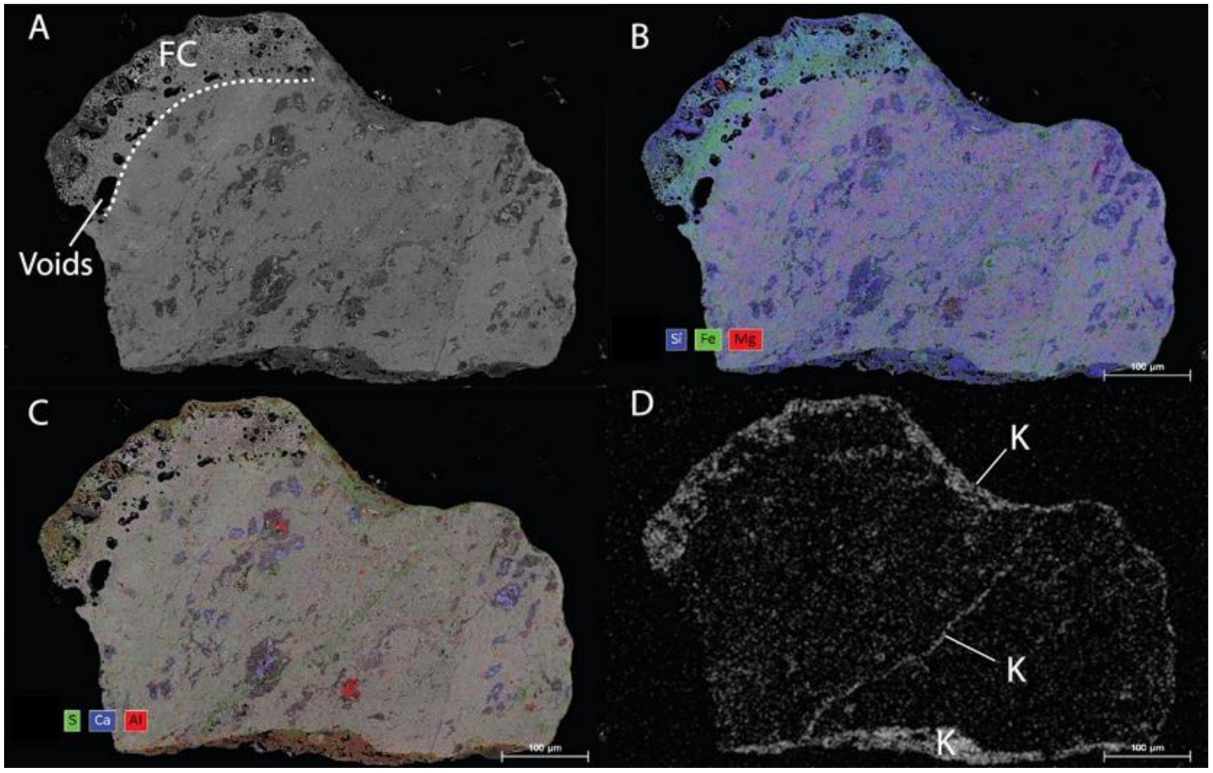

Fig. 5. EDX map of TAM5.29. A) Entire TAM5.29 particle. FC= Fusion Crust. B) Composite map showing Si-Fe-Mg abundances C) Composite map showing S-Ca-Al abundances. D) Map of K concentrations.

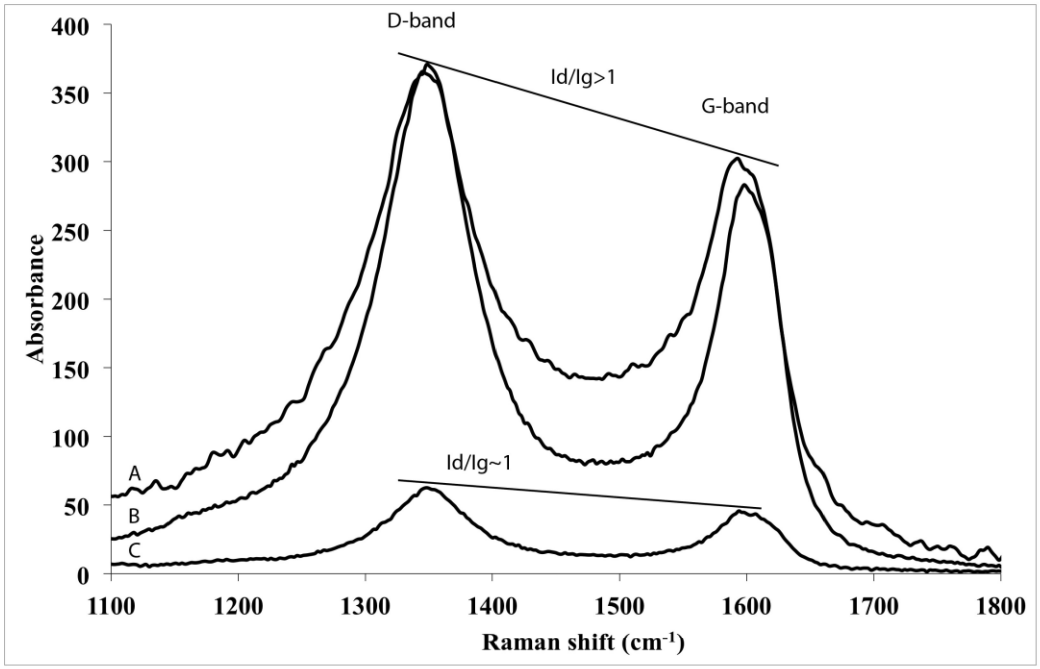

Fig. 6. D and G-bands of some representative analyses of TAM5.29. In case A and B D-band is higher than G-band giving a I_d/I_g ratio >1, indicating high carbon maturity and high metamorphic grade. In case C I_d/I_g ratio is ~1 related to a medium metamorphic grade.

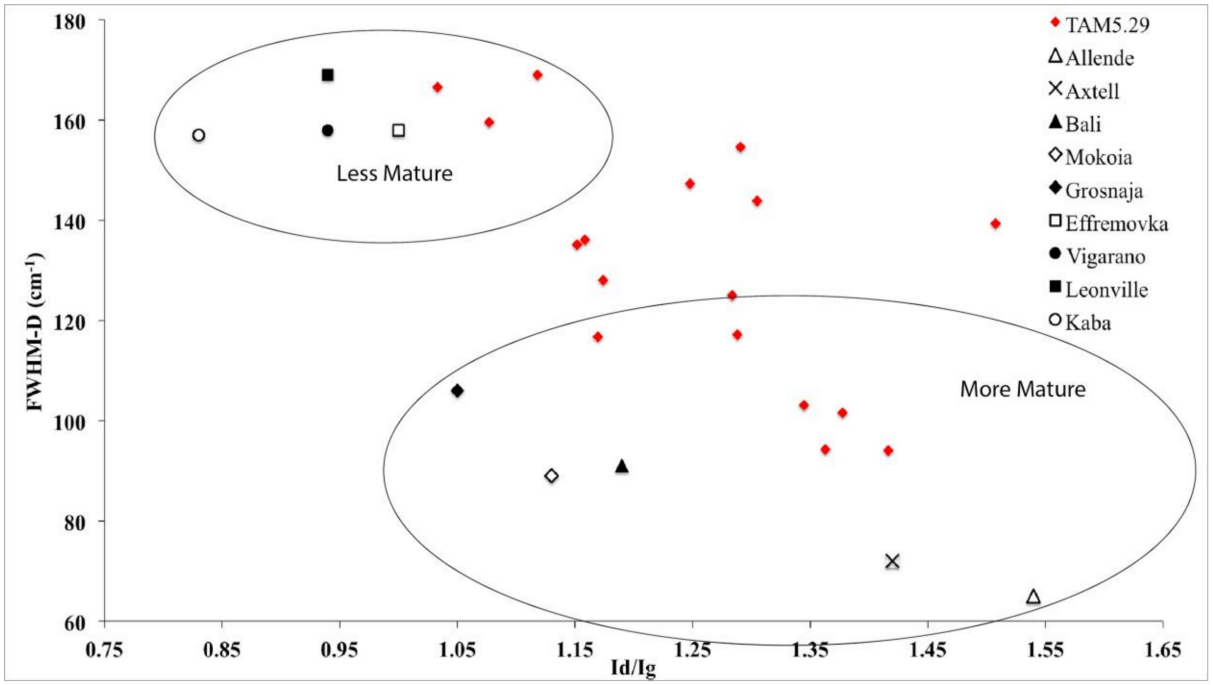

Fig. 7. Modified from Bonal et al. (2006). Id/Ig ratios are plotted versus FWHM of the D-band. The two groups represent more metamorphosed (more mature) and less metamorphosed (less mature) CVs. Red dots represent TAM5.29 spectral parameters.

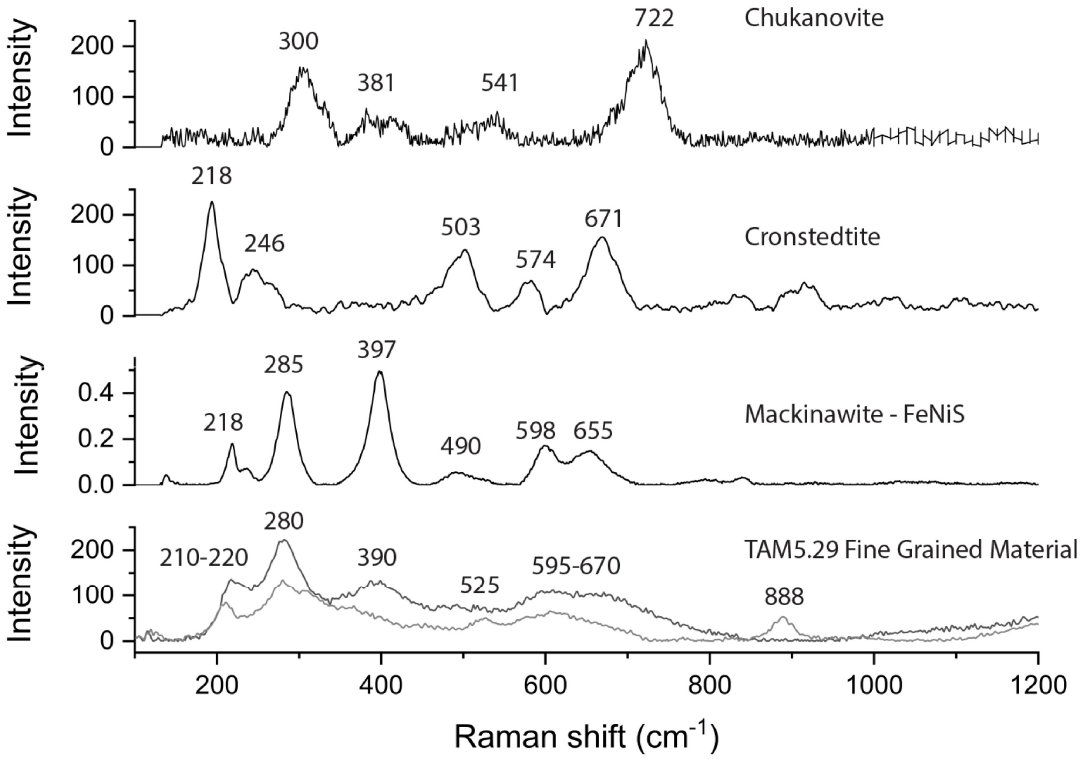

Fig. 8. Raman spectra of TAM5.29 fine-grained material compared to possible minerals that are contained within it.

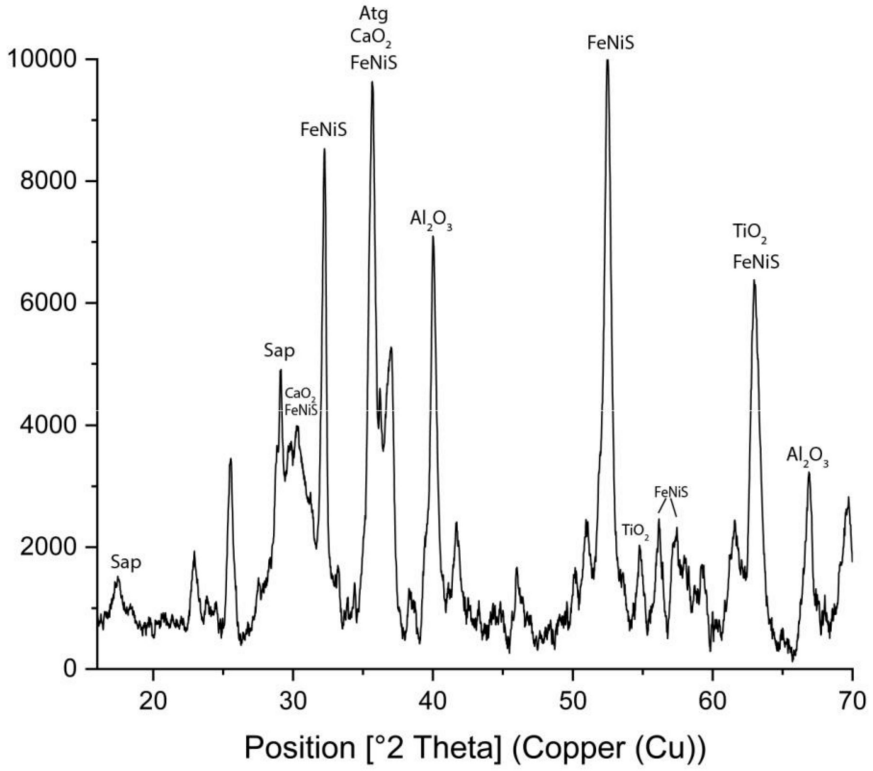

881
882 Fig. 9. µXRD analysis of TAM5.29. Sap: saponite; Atg: antigorite; FeNiS: iron-nickel sulfides (millerite and
883 mackinawite); CaO_2-Al_2O_3-TiO_2: oxides from CAIs that survived alteration. Sap=saponite, Atg=antigorite.
884

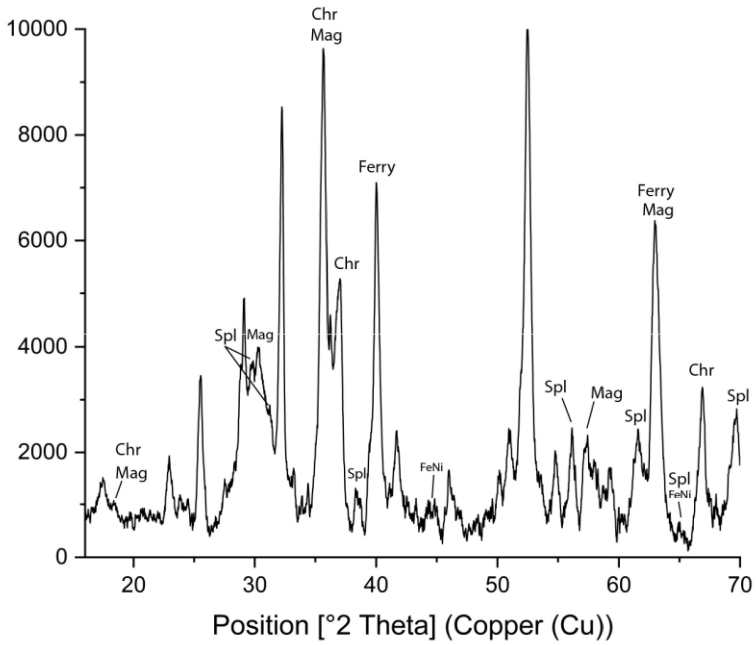

885
886
887 Fig. 10. µXRD analysis of TAM5.29. Mg: magnetite; Sp: spinel; FeNi: kamacite; Chr: chromite; Ferry:
888 ferrihydrite. Micron sized metal-oxide grains in TAM5.29, in agreement with EDS data in table S2, are mainly
889 magnetite, spinel, chromite and hydrated Fe-oxides such as ferrihydrite. Minor and rare FeNi alloys may be
890 also present. The fact that TAM5.29 mainly contains metal-oxides is also in agreement with µXRD data in fig. 9

where CaO_2-Al_2O_3-TiO_2 are found. Furthermore this confirms the affinity of TAM5.29 with the CVox group. Mag=magnetite, Spl=spinel, Ferry=ferrihydrite, FeNi=metal alloys.

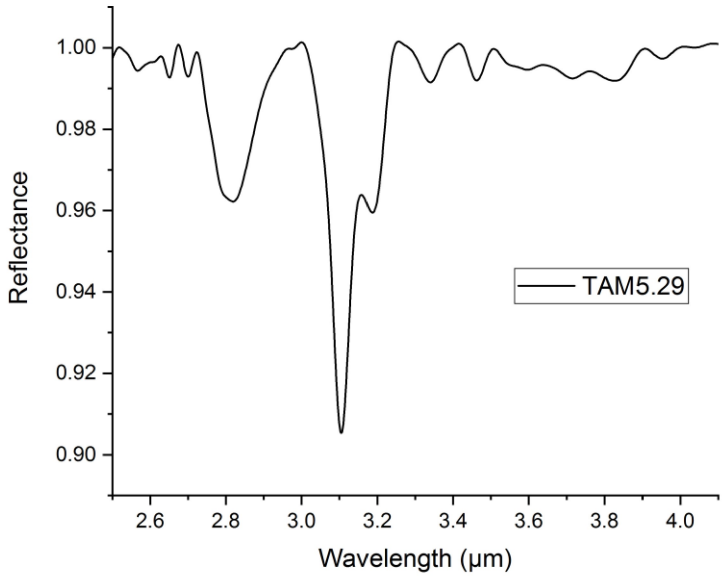

Fig. 11. IR reflectance spectra of TAM5.29. To be noticed the 2.8 µm band of Fe hydrous phyllosilicates, 3.3-3.4 µm band given by organic matter (i.e. CH compounds, aromatic and aliphatic hydrocarbons), a broad band between 3.6 and 3.8 µm likely related to SH functional groups and the 3.9 µm band of carbonates (likely Fe-carbonates). The 3.1 µm band is a very discussed band and attribution to a mineral phase is difficult, its nature will be discussed in a dedicated paper.

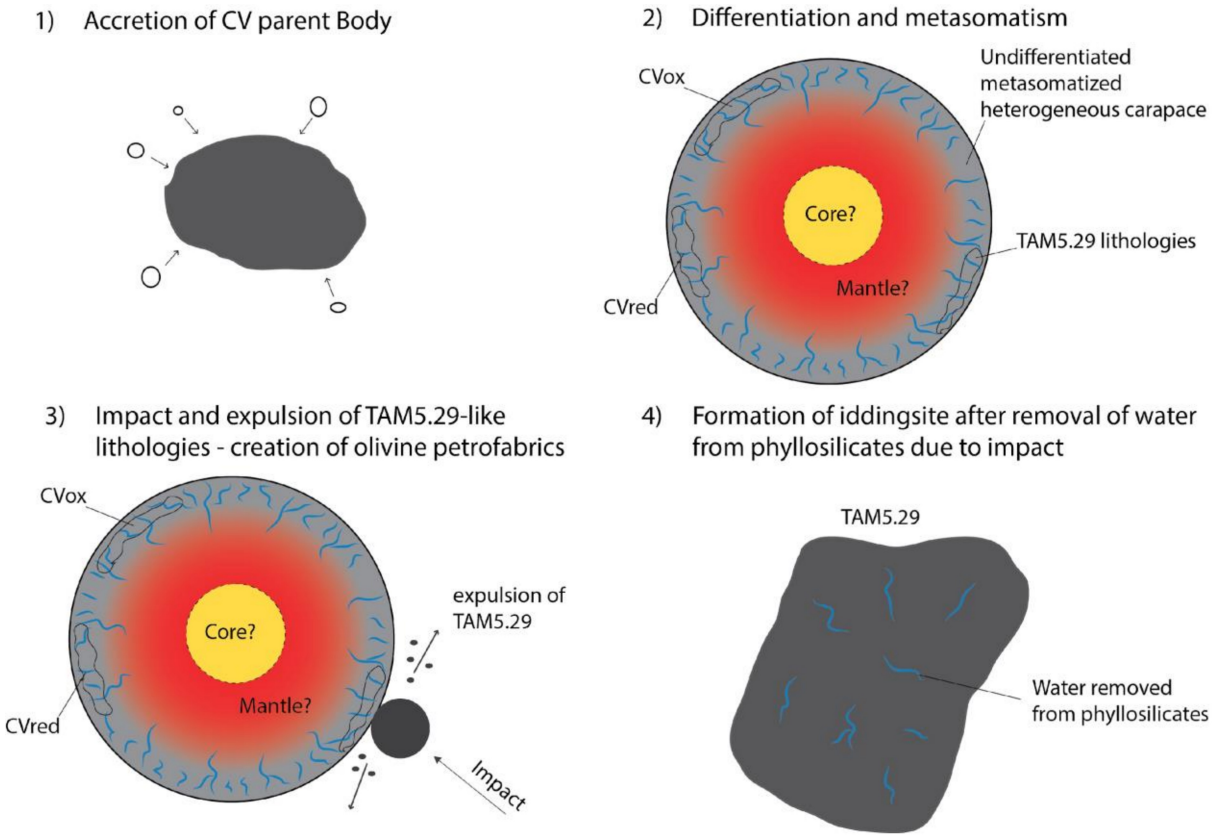

Fig. 12. Sketch representing stages of formation of TAM5.29. 1) Accretion of the CV parent body. 2) Differentiation into a core, mantle and an undifferentiated chondritic crust. The outer layer, or carapace, is heterogeneous in composition and suffer metasomatic alteration, hydrothermal activity and impact gardening. Different areas with different composition and environment cause the formation of the different types of CVs (CV_{ox}, CV_{red} and TAM5.29-like lithologies). 3) An impact occurs in the area where TAM5.29-like lithologies are found and TAM5.29 is expelled from the CV parent body. In this stage preferred orientation of olivine is created and the thermal metamorphism is terminated. 4) TAM5.29 is already separated from the parent body and water removed from hydrated minerals creates iddingsite at low temperature.

Supplementary Material

Table S1. Oxide (wt%) EDS analyses of olivine, pyroxene, andradite and spinel of the TAM5.29 micrometeorite.

	Olivine		Pyroxene		Andradite		Spinel	
	Mean	σ	Mean	σ	Mean	σ	Mean	σ
Na_2O	0.11	0.08	0.49	0.33	0.12	0.11	0.23	0.10
MgO	15.2	2.50	21.9	15.1	0.76	0.77	17.1	1.54
Al_2O_3	1.27	1.46	3.27	3.00	0.65	0.54	65.2	1.65
SiO_2	27.6	2.70	52.7	5.07	33.6	1.61	0.97	0.85
K_2O	n.d.	0.96	0.44	0.58	0.05	0.05	0.03	0.02
CaO	0.35	0.09	7.55	9.15	28.3	9.06	0.16	0.19
TiO_2	0.07	0.14	0.20	0.10	0.02	0.06	0.15	0.04
Cr_2O_3	0.13	0.13	0.75	0.68	0.04	0.06	0.28	0.04
MnO	0.11	2.78	0.15	-	4.58	11.6	0.09	0.06
FeO	44.3	0.12	12.8	11.8	27.0	1.81	15.6	2.06
NiO	0.19	-	n.d		n.d		0.06	0.06
Tot	89.3*		100.3		95.11*		99.82	
Fo/En	37.8	4.85	59.7	33.8				
Fa/Fs	62.0	4.85	24.0	24.6				
Wo			16.3	18.2				

n.d.: Not Determined

* Low total due to contamination of near-by hydrous minerals and inclusions of organic matter.

Table S2. Oxide wt% EDS analyses of metal oxides of TAM5.29. Due to the small size of the crystals (1-2 µm) analyses are contaminated by near-by phases giving high abundances of SiO_2 and S and low totals due to OH and C contamination. All analyses have high concentrations of Fe with the exception of Metal OX_5 that have high Cr instead. In all the analyses are also present minor quantities of Mg, Al and in Metal OX_5 also Ti. Thus, the most likely phases are: magnetite, chromite, spinel, ulvospinel etc.

	Metal OX_1	Metal OX_2	Metal OX_3	Metal OX_4	Metal OX_5
Na_2O	0.25	0.01	0.08	0.23	0.53
MgO	2.54	5.63	5.74	3.81	11.3
Al_2O_3	4.46	12.9	3.26	5.95	12.2
SiO_2	4.89	10.5	10.9	9.03	22.9
P_2O_5	n.d.	0.24	0.19	n.d.	0.72
S	0.32	2.83	1.46	1.59	7.92
K_2O	n.d.	0.24	n.d.	0.21	0.89
CaO	n.d.	0.20	0.14	0.02	0.65
TiO_2	n.d.	0.34	0.42	n.d.	2.50
Cr_2O_3	n.d.	0.76	0.30	0.21	24.5
MnO	n.d.	0.04	0.17	n.d.	n.d.
FeO	77.9	57.6	68.4	71.5	17.6
NiO	n.d.	0.11	0.01	0.01	n.d.
Tot	91.4	91.4	91.1	92.5	101.7

n.d.: Not Detected.

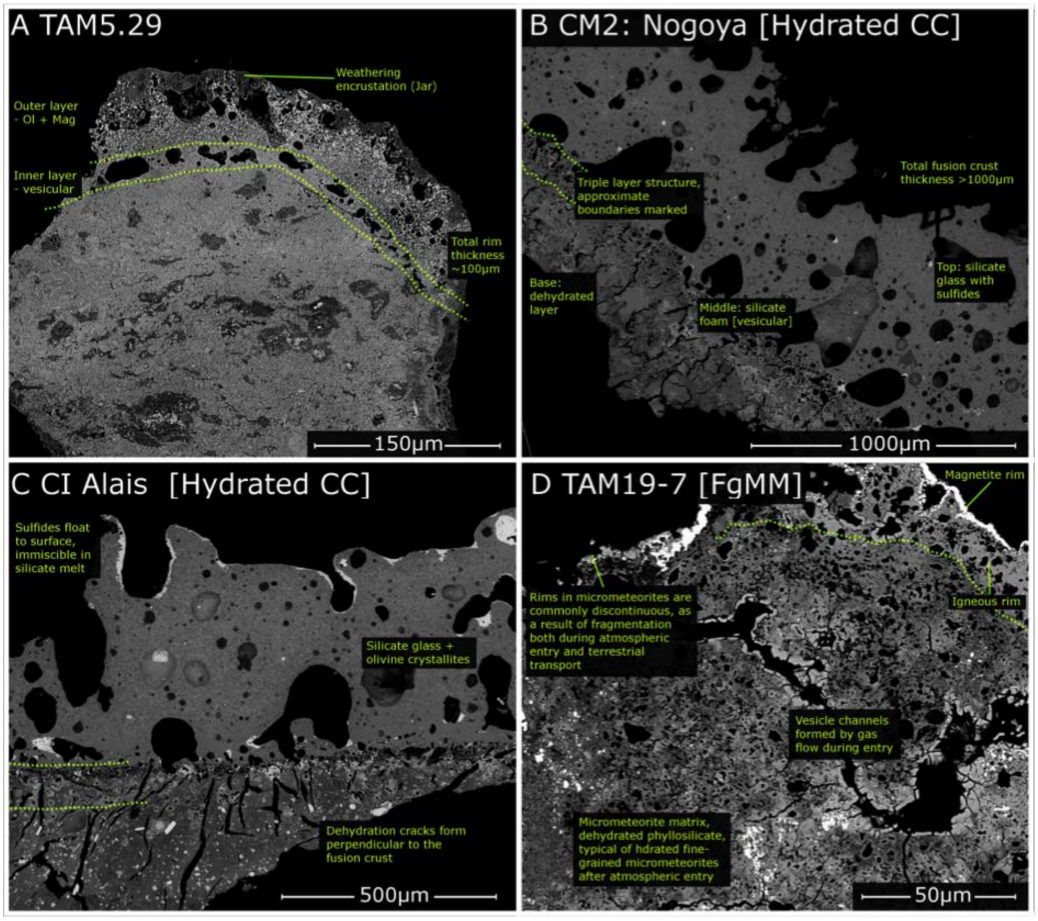

Fig.S1. The melt layer on TAM5.29 developed during atmospheric entry and comparison against fusion crusts and igneous rims on micrometeorites.